

# Wannier states and spin supersolid physics in the triangular antiferromagnet $\text{K}_2\text{Co}(\text{SeO}_3)_2$

M. Zhu,<sup>1,\*</sup> Leandro M. Chinellato,<sup>2,†</sup> V. Romerio,<sup>1</sup> N. Murai,<sup>3</sup> S. Ohira-Kawamura,<sup>3</sup> Christian Balz,<sup>4</sup> Z. Yan,<sup>1</sup> S. Gvasaliya,<sup>1</sup> Yasuyuki Kato,<sup>5</sup> C. D. Batista,<sup>2,6</sup> and A. Zheludev<sup>1,‡</sup>

<sup>1</sup>Laboratory for Solid State Physics, ETH Zürich, 8093 Zürich, Switzerland

<sup>2</sup>Department of Physics, The University of Tennessee, Knoxville, Tennessee 37996, USA

<sup>3</sup>J-PARC Center, Japan Atomic Energy Agency, Tokai, Ibaraki 319-1195, Japan

<sup>4</sup>ISIS Neutron and Muon Source, STFC Rutherford Appleton Laboratory, Didcot OX11 0QX, United Kingdom

<sup>5</sup>Department of Applied Physics, University of Fukui, Fukui 910-8507, Japan

<sup>6</sup>Quantum Condensed Matter Division and Shull-Wollan Center, Oak Ridge National Laboratory, Oak Ridge, Tennessee 37831, USA

(Dated: December 30, 2024)

We use a combination of ultra-high-resolution inelastic neutron scattering and Monte Carlo numerical simulations to study the thermodynamics and the structure of spin excitations in the spin-supersolid phase of the triangular lattice XXZ easy axis antiferromagnet  $\text{K}_2\text{Co}(\text{SeO}_3)_2$  and its evolution in a magnetic field. BKT transitions heralding the onset of Ising and supersolid order are detected. Above the supersolid phase the value of Wannier entropy is experimentally recovered. At low temperatures, with an experimental resolution of about  $23 \mu\text{eV}$ , no discrete coherent magnon modes are resolved within a broad continuum of scattering. In addition to gapless excitations, a pseudo-Goldstone mode with a small energy gap of  $0.06 \text{ meV}$  is found. A second excitation continuum is seen at higher energy, in place of single-spin-flip excitations of the Ising model. In applied fields the continuum gradually morphs into coherent spin waves, with the Goldstone and pseudo-Goldstone sectors showing distinct evolution. The agreement between experiment and numerical simulations is excellent on the quantitative level.

## I. INTRODUCTION

Identifying and understanding novel quantum phases of matter have been a central topic in modern condensed matter physics. The search for a supersolid, an exotic quantum state which is simultaneously a solid and a superfluid [1], is one of the most celebrated examples among such efforts. Originally proposed theoretically in solid helium [2, 3], the supersolid phase has since been studied extensively across various systems, including cold atoms [4–6], hard-core bosons [7–9], and quantum spin systems [10–14]. Despite significant theoretical progress, experimental identification of a supersolid phase remains a challenge.

The quantum  $S = 1/2$  antiferromagnetic XXZ spin Hamiltonian on a triangular lattice [15–17] presents a promising platform for realizing a supersolid state [18–20]. The “parent” Ising model has been famously solved by Wannier [21]. The ground state is macroscopically degenerate with no magnetic order and a residual entropy of  $0.323R$ . Members of this manifold are states where each triangle of the lattice carries two spins opposed to the third one. Since the model is classical, excitations are flat bands corresponding to flips of single spins. An ordered state is formed when this degeneracy is lifted by off-axial interactions in the XXZ model. The supersolid interpretation is based a one-to-one mapping between a

spin-1/2 magnet and a gas of hard-core bosons on the lattice [22]. In this mapping, the local magnetization along the  $z$ -axis,  $m_j^z$ , corresponds to the local boson density, while the magnitude and direction of the  $xy$  component of the local magnetization,  $m_j^{xy}$ , determine the amplitude and phase of the local Bose-Einstein condensate (BEC) order parameter. The “solid” spin ordering is associated with a colinear spin density wave along the  $z$ -axis, while the “BEC” translates into some form of  $XY$ -ordering.

The superfluid current of a bosonic gas in the BEC state corresponds to a superfluid spin current in the pure XXZ model. However, it is important to note that the spin Hamiltonian of a real spin system always includes terms that break the continuous symmetry associated with the conservation of any component of the net magnetization. Consequently, real spin systems lack a continuity equation, resulting in short-lived spin currents and making the concept of a spin superfluid poorly defined. Nevertheless, we will continue to use the term “spin supersolid” to describe spin systems that are well approximated by  $U(1)$ -invariant models, which undergo a transition into a “solid” phase at a critical temperature  $T_{c1}$ , followed by a second transition into a “superfluid” phase that coexists with the solid at a lower temperature  $T_{c2}$ . As we will see here, a key aspect that remains robust in the spin incarnation of this phenomenon is the strong quantum character of the low-energy excitations, which are not captured by a semi-classical  $1/S$  expansion.

Various theoretical approaches have predicted a spin supersolid ground state for easy-axis exchange anisotropy ( $0 < \alpha = J_{xy}/J_{zz} < 1$ ) [13, 16, 23–25]. The magnetic ordering exhibits a three-sublattice planar “Y”-spin struc-

\* These two authors contributed equally

† These two authors contributed equally; [lchinell@vols.utk.edu](mailto:lchinell@vols.utk.edu)

‡ [zhelud@ethz.ch](mailto:zhelud@ethz.ch); <http://www.neutron.ethz.ch/>

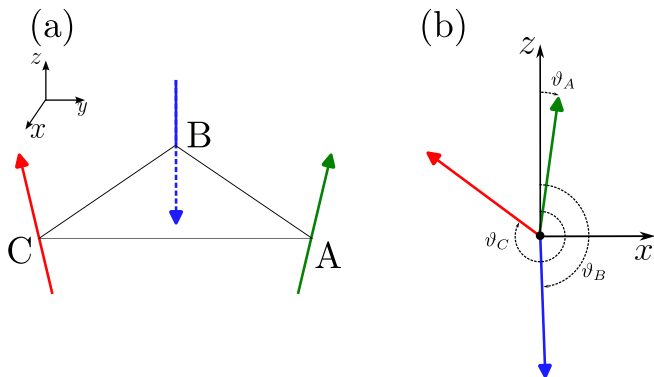


FIG. 1. (a) Classical Y-phase. The order breaks the  $U(1)$  symmetry of the Hamiltonian selecting one orientation on the  $xy$ -plane and the  $C_3$  lattice geometry selecting one sublattice for the spin down. (b) The classical ground state exhibits accidental continuous degeneracy due to the freedom to select one of the three spin angles, with the other two constrained by the derived relation Eq. 2.

ture, consisting of a commensurate spin density wave in the out-of-plane  $z$ -component with zero net magnetization, alongside an in-plane transverse  $xy$  moment. Notably, this “Y”-spin structure differs from the classical ordering for  $\alpha \ll 1$ , where the classical “Y” [see Figure 1(a)] structure has a net magnetization close to one-third of the saturation value. In contrast, quantum fluctuations significantly reduce the length of the two quasi-parallel spins to nearly half the length of the spin that is nearly anti-parallel to the other two. This strong quantum effect, driven by the macroscopic ground state degeneracy of the pure Ising model, suggests the possibility of highly non-classical spin dynamics. The system undergoes a quantum phase transition to a collinear up-down (uud) phase in a magnetic field ( $m/m_{\text{sat}} = 1/3$ ), whose spin dynamics is expected to be well described by a semi-classical theory [26, 27].

While the spin supersolid ground state is well understood theoretically, the spectrum of magnetic excitations remains an open question. Recent inelastic neutron scattering (INS) study on the triangular lattice easy-axis XXZ antiferromagnet  $\text{K}_2\text{Co}(\text{SeO}_3)_2$  [28] sheds new light on this issue. The ground state of  $\text{K}_2\text{Co}(\text{SeO}_3)_2$  has been proposed as a spin supersolid phase with a “Y” structure [28–30]. Interestingly, the spin dynamics is highly unusual, with the low-energy magnetic spectrum dominated by a broad continuum of excitations, aside from the gapless Goldstone modes, and a roton-like excitation dip observed at the M points of the Brillouin zone.

In stark contrast to the zero-field spectrum, the magnetic excitations in the field-induced uud plateau phase become sharp, resolution-limited magnons, well described by semiclassical spin wave theory [28]. Since excitation continua in frustrated magnets are often seen as indicators of proximity to a quantum spin liquid state [31–35], understanding the origin of this continuum in  $\text{K}_2\text{Co}(\text{SeO}_3)_2$  is crucial for exploring quantum dynamics

scenarios without a semiclassical counterpart.

In this article, we address this question by combining new ultra-high-resolution inelastic neutron scattering and additional thermodynamic measurements with numerical quantum Monte Carlo (QMC) simulations of a sign-problem-free low-energy model. In zero field, both in thermodynamics and in spectroscopy, we identify the energy scales that separate the “Wannier states” responsible for the formation of the supersolid state from high-energy excitations consisting of plaquettes with three parallel spins. We study the low-energy spectrum in the Wannier subspace  $\mathcal{W}$  to within an energy resolution of approximately  $23 \mu\text{eV}$ , putting experimental bounds on intensities and energies of any coherent excitations relative to the continuum. At the K-point, in addition to gapless excitations, we find an additional pseudo-Goldstone mode with a tiny gap of  $60 \mu\text{eV}$ . At higher energies of  $3 \text{ meV}$ , where flat spin flip modes are to be found in the Ising model, we observe a second structured and dispersive continuum. In applied fields, we follow the evolution of the low-energy excitations through the supersolid state and all the way to the uud phase boundary. The continuum coalesces into what eventually becomes sharp spin waves. The pseudo-Goldstone gap at the K point increases with magnetic field, even as the roton-like dip at the M point stays prominent. In contrast, the gapless excitations remain gapless until the quantum critical point, but their roton minimum quickly vanishes.

## II. MATERIAL AND METHOD

$\text{K}_2\text{Co}(\text{SeO}_3)_2$  is an easy-axis  $S = 1/2$  antiferromagnet very close to the Ising limit with  $\alpha = 0.08$  [28] deduced from high-field magnetometry measurements. At zero magnetic field, it exhibits no long-range magnetic order down to  $T = 0.35 \text{ K}$  [30]. Below that our calorimetric study revealed an additional low-temperature phase [28], which has been proposed to be the theoretically predicted spin-supersolid [16, 24]. When a magnetic field is applied along the easy axis, a quantum critical point is found at  $\mu_0 H_c = 0.8(1) \text{ T}$ , beyond which the system transitions into the uud plateau phase. Neutron diffraction studies have revealed quasi-two-dimensional magnetic reflections with propagation vectors  $(1/3, 1/3)$  in both the Y- and the uud phases, suggesting magnetic structures with a  $\sqrt{3} \times \sqrt{3}$  supercell qualitatively in agreement with the expected three-sublattice order in the spin-supersolid and spin-solid phase [28].

Single crystals of  $\text{K}_2\text{Co}(\text{SeO}_3)_2$  are grown as in Ref. [30]. The crystal structure contains ABC-stacked two-dimensional triangular lattice planes of  $\text{Co}^{2+}$  ions separated by K layers [Figure 2]. The space group is  $R\bar{3}m$ , and the lattice parameters are  $a = 5.52 \text{ \AA}$ , and  $c = 18.52 \text{ \AA}$  [36]. High-resolution inelastic neutron scattering measurements were performed using the AMATERAS cold-neutron time-of-flight spectrometer [37] in J-PARC, Japan. The incident neutron energies used are

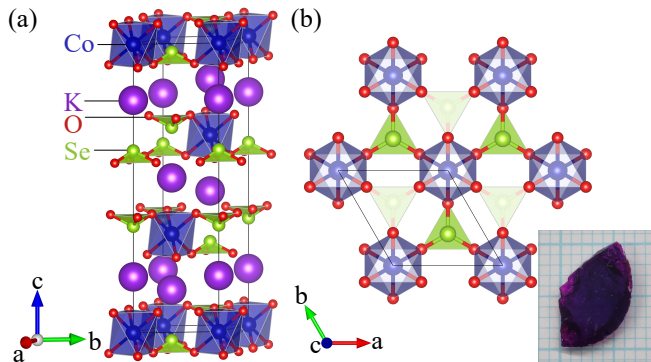


FIG. 2. A schematic view of the crystal structure of  $\text{K}_2\text{Co}(\text{SeO}_3)_2$ . (a) Unit cell with ABC-stacked triangular planes of  $\text{Co}^{2+}$  ions. (b) Top view of a single triangular plane. Inset: photo of a  $\text{K}_2\text{Co}(\text{SeO}_3)_2$  single crystal on a millimeter grid paper.

$E_i = 1.69$  and  $7.73$  meV. The energy resolution at elastic scattering is  $23$  and  $240$   $\mu\text{eV}$ , respectively. The data were collected by rotating the sample by  $160$  degrees with  $1$  degree per step, and analyzed using the Horace package [38]. Inelastic neutron scattering measurements in a magnetic field were carried out using the LET cold-neutron time-of-flight spectrometer in ISIS facility, Rutherford Appleton Laboratory, United Kingdom. The incident neutron energy is fixed at  $E_i = 2.15$  meV. The spectrometer is operated in the high-flux mode, with chopper frequency  $240/120$  Hz, yielding an energy resolution of  $40$   $\mu\text{eV}$  at elastic scattering. The data were obtained by rotating the sample by  $90$  degrees with  $1$  deg per step. A single crystal sample of  $425$  mg and  $1.23$  grams were used for AMATERAS and LET, respectively. They are mounted on a copper holder and cooled using a  $^3\text{He}/^4\text{He}$  dilution refrigerator. At LET, a magnetic field is applied along the  $[0,0,1]$  direction using a vertical-field cryomagnet. In both cases the sample was oriented with  $[1,0,0]$  and  $[0,1,0]$  directions in the horizontal plane. The specific heat measurements were performed using a relaxation method by a Quantum Design Physical Property Measurement System on a  $0.05$  mg single-crystal sample for  $0.12$ – $4$  K with a dilution fridge insert and on a  $3.95$  mg one for  $2$ – $300$  K.

All LSWT calculations were performed using Sunny.jl [39], worldline QMC calculations were performed using a modified directed-loop algorithm [40, 41] for system sizes of  $36 \times 36$  (thermodynamic properties) and  $72 \times 72$  (spin dynamics). The analytic continuation of the QMC data was carried out using the SmoQyDEAC.jl library [42, 43].

### III. MODEL AND THEORY

In the study of real magnetic systems, we encounter two key challenges: extracting a model that accurately describes the most relevant aspects of the system’s physics, and then solving it. This task is “ouroboric” in

nature, as determining the model’s parameters requires solving it first and comparing the results with experimental observations. Since most models cannot be solved exactly, this makes the process highly non-trivial. A reasonable approach is to propose a minimal model that captures the essential physical features of the system, at least within a certain energy scale, and solve it using well-justified approximations. Following this methodology, and building on the results outlined in the introduction and in our previous work [28], we propose modeling the magnetic properties of  $\text{K}_2\text{Co}(\text{SeO}_3)_2$  using an XXZ Hamiltonian,

$$\mathcal{H} = \sum_{\langle i,j \rangle} [J_{zz} S_i^z S_j^z + J_{xy} (S_i^x S_j^x + S_i^y S_j^y)] - h \sum_i S_i^z, \quad (1)$$

where  $h = g\mu_B\mu_0 H$ ,  $\mu_0 H$  is the external magnetic field,  $\mu_B$  is the Bohr magneton and  $g = 7.9$  the Landé g-factor. The exchange interactions determined in [28] through high-field magnetometry measurements were further refined by detailed comparison with theoretical calculations, as discussed in the following section. This process yielded updated values of  $J_{zz} = 3.1$  meV,  $J_{xy} = 0.217$  meV, and an anisotropy ratio of  $\alpha = J_{xy}/J_{zz} = 0.07$ . The refinement was essential to achieve a precise agreement with the specific heat and magnetization curves presented in subsequent sections.

Let us first highlight the classical and semi-classical predictions of this model and evaluate how well they align with experiments. In the strictly Ising limit ( $J_{xy} = 0$ ) and in the absence of the external magnetic field ( $\mu_0 H = 0$ ), the Hamiltonian becomes a triangular lattice Ising model, exhibiting an extensively degenerate ground state manifold [21]. The ground state subspace is spanned by configurations where no triangular plaquette has all three spins aligned in parallel. In the introduction, we referred to this subspace as the “Wannier space”  $\mathcal{W}$ . An infinitesimal magnetic field applied along the  $z$ -direction lifts the degeneracy and favors three possible “uud” ground states, where two spin sublattices align parallel to the field, and the third sublattice has spins oriented antiparallel to the field. This implies that the magnetization changes discontinuously from zero to one-third of the saturation value.

As we move away from the Ising limit  $J_{xy} \ll J_{zz}$  in the absence of the external field, the ground state manifold of the classical spin ( $S \rightarrow \infty$ ) Hamiltonian is two-dimensional. The first dimension emerges from the continuous  $U(1)$  symmetry associated with global spin rotations around the  $z$ -axis. The second dimension arises from an accidental continuous degeneracy, which corresponds to the freedom in selecting one of the three polar angles for the spins within the magnetic unit cell [44, 45]. These angles, measured with respect to the  $z$ -axis as illustrated in Figure 1(b), satisfy the following relationships,

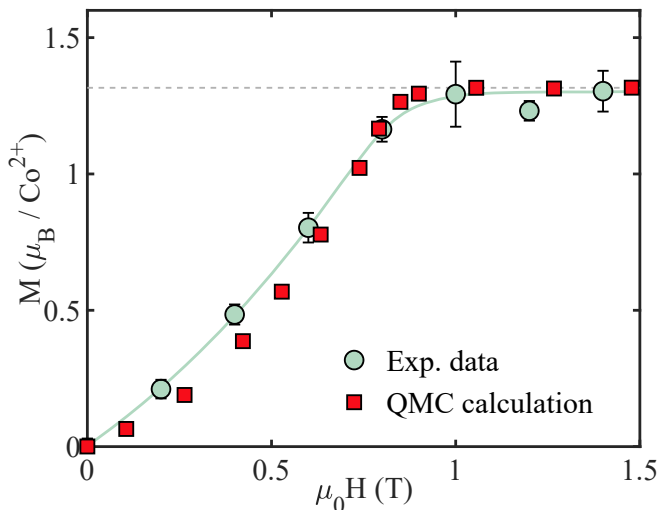


FIG. 3. Magnetization of  $\text{K}_2\text{Co}(\text{SeO}_3)_2$  as a function of applied field at  $T = 0.19$  K. Circles are experimental data from Ref. [28]. The solid curve is a guide for the eye. Red squares are QMC results (this work). The dashed line represents one-third of the experimental saturation magnetization.

$$\begin{aligned}
 \vartheta_B &= \varepsilon + \delta, & \vartheta_C &= \varepsilon - \delta \\
 \cos \delta &= \frac{\alpha}{(1 + \alpha)[\sin^2 \vartheta_A + \alpha \cos^2 \vartheta_A]^{1/2}} \\
 \cos \varepsilon &= \frac{\alpha \cos \vartheta_A}{[\sin^2 \vartheta_A + \alpha \cos^2 \vartheta_A]^{1/2}}
 \end{aligned} \quad (2)$$

with  $\vartheta_A$  arbitrarily chosen. The application of an infinitesimal magnetic field along the  $z$ -direction lifts the accidental degeneracy, selecting the Y-shaped ground state configuration depicted in Figure 1(a).

Although the classical ground state of the Hamiltonian in Eq. 1 qualitatively matches the state of  $\text{K}_2\text{Co}(\text{SeO}_3)_2$ , it completely fails to predict the zero-field magnetization. The classical solution yields a magnetization of

$$\frac{M}{M_{\text{sat}}} = \frac{1}{3} \frac{(J_{zz} - J_{xy})}{(J_{zz} + J_{xy})} \xrightarrow{\alpha \ll 1} \frac{1}{3} \quad (3)$$

which strongly contrasts with the zero magnetization observed experimentally, as shown in Figure 3. The absence of ground-state magnetization can be attributed to a significant reduction in the magnitude of the two quasi-parallel spins, approximately by a factor of two. However, such a pronounced reduction—resulting in the ordered moment being only 50% of its full value—indicates that quantum corrections are not adequately captured by a perturbative  $1/S$  expansion. Although we cannot entirely rule out the possibility of antiferromagnetic interlayer correlations characterized by  $J_{\perp}$ , the absence of a jump or noticeable change in the slope of the magnetization curve suggests that each individual layer has zero net magnetization.

Kleine *et al.* [44] demonstrated that quantum fluctuations lift the classical accidental ground state degeneracy by stabilizing the coplanar Y-order. This ordering pattern breaks two symmetries simultaneously: it spontaneously breaks the continuous  $U(1)$  symmetry of global spin rotations by selecting a specific orientation in the  $xy$ -plane, and it breaks the discrete  $C_3$  lattice symmetry (corresponding to  $2\pi/3$  rotations) by designating one of the three sublattices to host the minority spin. Notably, in the absence of a magnetic field, there is an additional breaking of time-reversal  $Z_2$  symmetry, corresponding to the up or down orientation of the minority spin. It is interesting to explore the consequences of these different symmetry breakings for the expected thermodynamic phase transitions in the pure 2D model.

In view of the distinct energy scales governing the stabilization of Ising (solid) and XY (BEC) orderings, it is clear that the solid or Ising ordering, characterized by the spontaneous breaking of  $C_3 \otimes Z_2$  symmetry at zero field and  $C_3$  symmetry at finite field, should occur at a higher critical temperature. At zero field, we expect this solid ordering to emerge through a sequence of two Berezinskii-Kosterlitz-Thouless (BKT) transitions, with  $T_{\text{BKT},1} > T_{\text{BKT},2}$ . A critical phase exists for  $T_{\text{BKT},2} < T < T_{\text{BKT},1}$ , while a massive phase with long-range Ising order develops for  $T < T_{\text{BKT},2}$  [46].

The behavior changes significantly in the presence of a finite magnetic field, where only the  $C_3$  symmetry is broken. Under these conditions, the critical phase acquires long-range Ising order and merges with the massive phase below  $T_{\text{BKT},2}$ . The two BKT transitions are replaced by a single second-order phase transition in the 2D Potts universality class at temperature  $T_{c1}$ . As the magnetic field approaches zero,  $T_{c1}$  converges to  $T_{\text{BKT},1}$ . Lastly, the XY order parameter is expected to undergo a BKT transition at a much lower temperature,  $T_{\text{BKT},3} \ll T_{\text{BKT},2}$ . When finite inter-layer coupling is included, the transition evolves into a three-dimensional XY phase transition, resulting in a phase with long-range XY order. Consequently,  $\text{K}_2\text{Co}(\text{SeO}_3)_2$  is expected to exhibit weak thermodynamic signatures of these phase transitions at zero field, particularly in measurements of specific heat ( $C_v$ ). Figure 4(a) presents the zero-field specific heat of  $\text{K}_2\text{Co}(\text{SeO}_3)_2$  measured up to high temperatures (open circles). The phonon contribution is approximated by the measured specific heat of the isostructural nonmagnetic counterpart  $\text{K}_2\text{Mg}(\text{SeO}_3)_2$  (solid squares). An empirical scale factor of 1.08 was applied in order to match the heat capacities of the two systems in the temperature range 50–100 K. The magnetic heat capacity  $C_{\text{mag}}$  of  $\text{K}_2\text{Co}(\text{SeO}_3)_2$  is plotted as a function of temperature in Figure 4(b). Here the phonon contribution and a nuclear Schottky feature at the lowest temperatures were subtracted from the total heat capacity. Signatures of three BKT transitions are observed (dashed lines), which are well aligned with the theoretical predictions.

While thermal fluctuations can be qualitatively captured by a classical spin model, the same does not hold

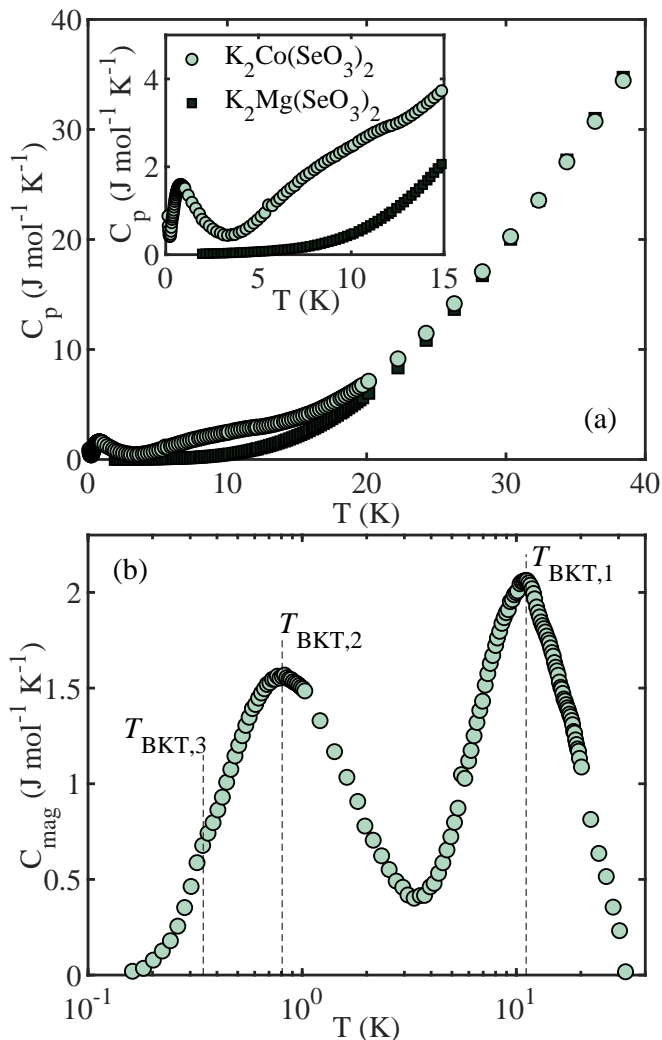


FIG. 4. (a) Heat capacity measured in  $\text{K}_2\text{Co}(\text{SeO}_3)_2$  (shaded circles) and in the non-magnetic counterpart  $\text{K}_2\text{Mg}(\text{SeO}_3)_2$  (solid squares) as a function of temperature. (b) Temperature dependence of the magnetic contribution to specific heat in  $\text{K}_2\text{Co}(\text{SeO}_3)_2$ . The phonon contribution was estimated based on the  $\text{K}_2\text{Mg}(\text{SeO}_3)_2$  data. A 1.08 scale factor was applied to the latter, to match the heat capacities of the two materials in the range 50 to 100 K. The two prominent peaks correspond to the two higher-temperature BKT transitions. A weaker feature at low temperature marks the third transition. Note the logarithmic temperature scale. Actual BKT transition temperatures are typically lower than the corresponding specific heat maximum [47].

true for quantum fluctuations. Using a simple spin-wave calculation, Kleine observed a substantial reduction in the total ground-state magnetization, nearly driving it to zero. While this result aligns closely with expectations for the quantum  $S = 1/2$  limit, it also raises concerns about the validity of the  $1/S$  expansion. Specifically, the first quantum correction to the dipole moment renormalization is nearly as large as the full moment, highlighting the limitations of this approach in effectively addressing

the problem.

At low energies,  $\omega \sim J_{xy}$ , the spin-wave calculation predicts two degenerate magnon bands: one corresponding to a true Goldstone mode associated with the broken  $U(1)$  symmetry, and the other a pseudo-Goldstone mode arising from the accidental continuous degeneracy of the classical ground state [see solid lines in Figure 5]. A third, nearly dispersionless band (not shown in the Figure) appears at higher energies,  $\omega \sim J_{zz}$ . In the  $S = 1/2$  limit, this mode corresponds to excitations into states in the subspace  $\mathcal{W}^\perp$ , which is orthogonal to the Wannier subspace  $\mathcal{W}$ .

Higher-order  $1/S$  corrections are expected to gap out the pseudo-Goldstone mode [48]. This is in qualitative agreement with our ultra-high-resolution inelastic neutron scattering measurement at the AMATERAS spectrometer using an incident neutron energy  $E_i = 1.69$  meV (more discussions in Sec. V), where a tiny energy gap of  $60 \mu\text{eV}$  is detected at the K point [Figure 5 inset]. However, the comparison of the linear spin wave theory (LSWT) dispersion with the INS data in Figure 5 and the strong reduction of the ordered moment suggests that the  $1/S$  expansion is insufficient to accurately capture the dispersion and spectral weight distribution of shorter-wavelength excitations. Consequently, we will adopt an alternative approach to account for the non-perturbative effects of strong quantum fluctuations.

Since our approach is based on a perturbative expansion in a different small parameter,  $J_{xy}/J_{zz}$ , it is essential to first verify that the excitation spectrum of  $\text{K}_2\text{Co}(\text{SeO}_3)_2$  exhibits two well-separated energy scales. This separation should be evident in the measured temperature dependence of the entropy. As calculated by Wannier, the zero-point entropy density of the pure Ising model is approximately  $\Delta S/R \approx 0.323$ , which is about half of  $\ln 2$ —the saturation entropy for a spin- $1/2$  system.

At zero field and temperature, quantum fluctuations induced by first-order corrections in  $J_{xy}$  remove the extensive ground state degeneracy by selecting the above discussed ground state sub-manifold within the Wannier subspace. The Wannier entropy should then be recovered at a crossover temperature  $T = T_{\text{cr}}$  of order  $J_{xy}/k_B$  and the entropy curve

$$\Delta S(T) = \int_0^T \frac{C_v}{T'} dT' \quad (4)$$

should exhibit a plateau at this temperature. Experimentally,  $\Delta S(T)$  of  $\text{K}_2\text{Co}(\text{SeO}_3)_2$  is obtained by integrating from the lowest temperature measured, as plotted against temperature in Figure 6. A plateau is observed, which confirms this separation of energy scales and reveals the value of the crossover temperature  $T_{\text{cr}} \simeq 2.5$  K. The relatively narrow temperature range of the observed plateau can be attributed to the moderate separation of energy scales, with  $J_{xy}$  being only ten times smaller than  $J_{zz}$ .

By exploiting this separation of energy scales, we derive a low-energy effective model  $\mathcal{H}_{\text{eff}}$  through degenerate perturbation theory to first order in  $J_{xy}$ . Our ap-

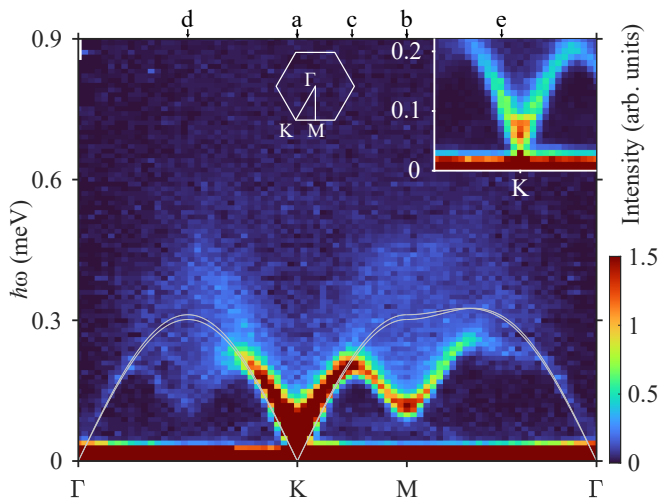


FIG. 5. False-color plot of inelastic neutron scattering intensity measured in  $\text{K}_2\text{Co}(\text{SeO}_3)_2$  in zero applied field and  $T = 0.07$  K as a function of energy and wave vector transfers along high-symmetry directions. The incident neutron energy is  $E_i = 1.69$  meV. The energy resolution is  $23 \mu\text{eV}$  at the elastic line. This is to be compared to the  $36 \mu\text{eV}$  resolution of the experiments described in Ref. [28]. The data are integrated over  $\pm 0.5$  r.l.u. in  $l$  and  $\pm 0.05$  r.l.u. in the  $(h, k, 0)$  plane perpendicular to the cut, and averaged over equivalent paths shown in Fig. 20. No background has been subtracted. Both longitudinal and transverse spin fluctuations contribute to scattering, the intensity being proportional to  $S^{zz}(\mathbf{q}, \omega) + S^{\perp\perp}(\mathbf{q}, \omega)$ . White solid lines are the dispersion curves calculated by linear spin wave theory. The white hexagon represents the Brillouin zone boundary.  $\Gamma$ , K and M label high symmetry points in the reciprocal space. Inset: a zoom-in view of the low-energy spectrum near the K point with a different color scale to highlight the gapped pseudo-Goldstone excitation. Labels on the top axis indicate the position of energy cuts shown in Figure 11.

proach is based on the observations initially made by A. Sen *et al.* [49] for the non-frustrated case and subsequently generalized by Fa Wang and collaborators [50]. The derivation begins by projecting the original Hamiltonian in Eq. (1) onto the Wannier subspace  $\mathcal{W}$  to produce an effective low-energy model. Wang *et al.* demonstrate the existence of a unitary transformation that reverses the sign of the  $xy$  term of the *effective low-energy model* while preserving both the eigenvalue spectrum and the diagonal correlation functions in the  $S^z$  basis. This transformation yields a Hamiltonian free from the sign problem, enabling the use of QMC simulations to compute both static and dynamic properties. In the following section, we detail this unitary transformation.

Since the Hilbert space of the effective low-energy model is the Wannier subspace  $\mathcal{W}$ , it is first necessary to introduce a suitable algebra of operators that act on this highly constrained space. This is achieved by introducing dimer coverings on the dual honeycomb lattice. As shown in Figure 7(a) and (b), a dimer is placed on the dual link perpendicular to each frustrated bond (a

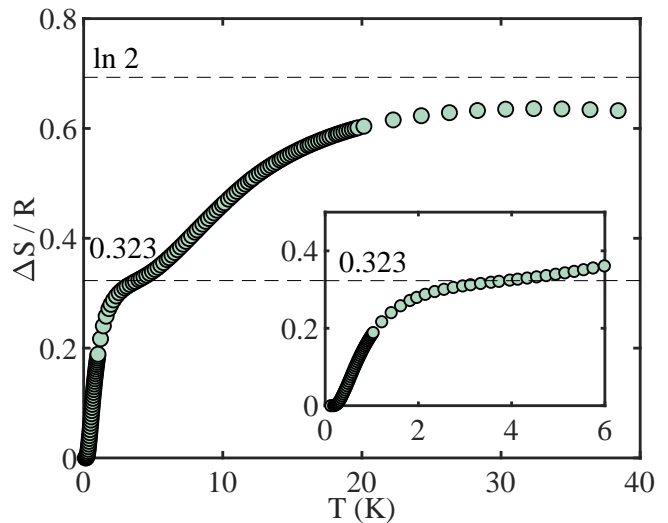


FIG. 6. Temperature dependence of magnetic entropy in  $\text{K}_2\text{Co}(\text{SeO}_3)_2$  in zero applied field, as obtained by integrating the measured specific heat and subtracting the phonon contribution determined from experiments on  $\text{K}_2\text{Mg}(\text{SeO}_3)_2$ . The dashed lines indicate the Wannier entropy and the expected high-temperature value  $\ln 2$ . The inset provides a zoomed-in view to highlight the plateau at the Wannier entropy. The 10% discrepancy between the high-temperature data and the expected saturation value is attributed to imperfect phonon subtraction. This effect is expected to be much smaller at temperatures below 10 K.

bond connecting two parallel spins) of a given spin configuration. We denote a specific dimer covering by  $\mathcal{C}$ . Because we are focusing on only one of the two states related by time-reversal symmetry, the proposed duality transformation results in a 2:1 mapping.

In this language,  $\mathcal{H}_{\text{eff}}$  is simply a quantum dimer model with a ring-exchange term that acts on each pair of adjacent hexagons on the dual honeycomb lattice (corresponding to each bond  $\langle i, j \rangle$  of the triangular lattice).

$$\mathcal{H}_{\text{eff}} = \frac{J_{xy}}{2} \sum_{\langle\langle ij \rangle\rangle} (|\infty_{\langle ij \rangle}\rangle \langle\infty_{\langle ij \rangle}| + h.c.) \quad (5)$$

In other words,  $\mathcal{H}_{\text{eff}}$  connects basis states that present a double-hexagon resonance as sketched in Figure 7(c). The ground state is then obtained by optimizing the energy gain produced by this dimer resonance.

The most general eigenstate of the effective Hamiltonian is written as a linear superposition of the different dimer coverings,

$$|\Psi_\alpha\rangle = \sum_{\{\mathcal{C}\}} \phi_\alpha(\mathcal{C}) |\mathcal{C}\rangle \quad (6)$$

with  $\langle \mathcal{C}' | \mathcal{C} \rangle = \delta_{\mathcal{C}'\mathcal{C}}$  and  $\sum_{\mathcal{C}} |\phi_\alpha(\mathcal{C})|^2 = 1$ . If a unitary transformation  $\hat{U}$  exists that changes the sign of  $\mathcal{H}_{\text{eff}}$ , the low-energy model can be mapped to the one that is for

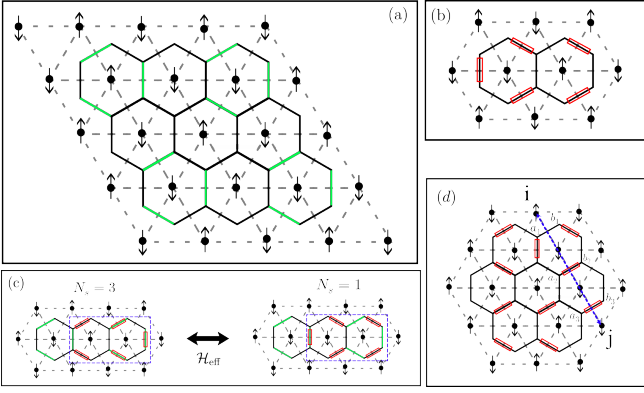


FIG. 7. a) Triangular lattice (dashed line) and the associated honeycomb dual lattice (bold line). The green bonds denote the “special” ones used in the unitary transformation. b) A resonant hexagon, the red boxes represent the bonds covered by a dimer. c) Effect of the Hamiltonian over a resonant hexagon, denoted by the blue box, and the number of special bonds covered by dimers  $N_s$ . d) Representation of the calculation of  $\langle S_i^z S_j^z \rangle$ , for  $ij$  connected by the blue dashed line. Since the line crosses for an odd number (1) of non-covered bonds in the dual lattice the correlator takes a negative value, as is expected by inspection.

negative  $J_{xy}$ , i.e., non-frustrated XY interaction. Consider the lattice depicted in Figure 7(a), where specific bonds—designated as “special”—are marked with green lines. For any given dimer covering  $\mathcal{C}$ , we define  $N_s(\mathcal{C})$  as the number of special bonds occupied by dimers. As illustrated in Figure 7(c), a resonance within any resonant hexagon changes  $N_s(\mathcal{C})$  by  $\pm 2$ . To capture this behavior, we introduce the following unitary transformation on the dimer basis [50]:

$$|\mathcal{C}'\rangle := \hat{U}|\mathcal{C}\rangle = i^{N_s(\mathcal{C})}|\mathcal{C}\rangle \quad (7)$$

where  $i$  is the imaginary unit. Consequently, basis elements connected by  $\mathcal{H}_{\text{eff}}$  differ in their  $N_s$  values by integer multiples of  $\pm 2$ . Defining  $|\Psi'_\alpha\rangle = \hat{U}|\Psi_\alpha\rangle$ , we obtain

$$\begin{aligned} \langle \Psi'_\gamma | \mathcal{H}_{\text{eff}} | \Psi'_\alpha \rangle &= \sum_{\{\mathcal{C}\}} -i^{N_s(\mathcal{C}')} i^{N_s(\mathcal{C})} \phi_\gamma^*(\mathcal{C}') \phi_\alpha(\mathcal{C}) \langle \mathcal{C}' | \mathcal{H}_{\text{eff}} | \mathcal{C} \rangle \\ &= \sum_{\{\mathcal{C}\}} i^{\pm 2} \phi_\gamma^*(\mathcal{C}') \phi_\alpha(\mathcal{C}) \langle \mathcal{C}' | \mathcal{H}_{\text{eff}} | \mathcal{C} \rangle \\ &= \sum_{\{\mathcal{C}\}} -\phi_\gamma^*(\mathcal{C}') \phi_\alpha(\mathcal{C}) \langle \mathcal{C}' | \mathcal{H}_{\text{eff}} | \mathcal{C} \rangle \\ &= \langle \Psi_\gamma | -\mathcal{H}_{\text{eff}} | \Psi_\alpha \rangle, \end{aligned} \quad (8)$$

implying that  $\hat{U}$  maps  $\mathcal{H}_{\text{eff}}$  into  $-\mathcal{H}_{\text{eff}}$  without affecting the structure of the wave function. Since the unitary transformation preserves the energy spectrum, thermodynamic properties, which depend solely on the energy eigenvalues, remain unchanged.

Consider the spin-spin correlation function  $\langle S_i^z S_j^z \rangle$ . As illustrated in Figure 7(d), a line connecting sites  $i$  and  $j$

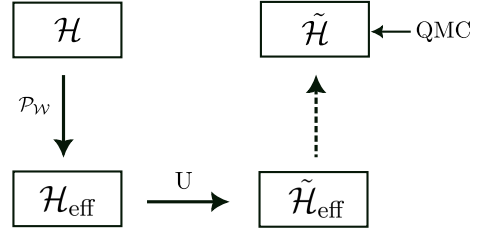


FIG. 8. Sketch of the strategy used to attack the present problem.  $\mathcal{P}_W$  represent the projection of the full Hamiltonian over the Wannier space to arrive to a low energy Hamiltonian  $\mathcal{H}_{\text{eff}}$ , that is mapped by the unitary transformation  $U$  to a non-frustrated Hamiltonian  $\tilde{\mathcal{H}}_{\text{eff}}$ . We promote  $\tilde{\mathcal{H}}_{\text{eff}}$  to  $\tilde{\mathcal{H}}$  in the complete Hilbert space and solve it using QMC.

intersects a set of honeycomb lattice edges  $\langle ab \rangle$ . The value of  $S_i^z S_j^z$  depends on the parity of unoccupied edges along this line: it equals  $+S^2$  when the number of intersected edges without dimers is even, and  $-S^2$  when this number is odd. Now, define the dimer number operator  $\hat{n}_{ab} := (1 + 4S_i^z S_j^z)/2$  where  $ab$  refers to the honeycomb lattice edge dual to the triangular lattice edge  $ij$ . Using this operator, the correlation function becomes a non-local string operator, expressed as:

$$\langle S_i^z S_j^z \rangle = \frac{1}{4} \left\langle \prod_{\substack{\langle ab \rangle \\ \text{cut by } ij}} (2\hat{n}_{ab} - 1) \right\rangle. \quad (9)$$

The product has  $2^{|j-i|}$  terms (with  $|j-i|$  being the distance between  $j$  and  $i$  measured in units of the triangular lattice constant). These terms can be evaluated using the Grassmannian integral method. Because these operators are diagonal in the dimer basis,  $\langle \Psi' | S_i^z(t) S_j^z(0) | \Psi' \rangle = \langle \Psi | S_i^z(t) S_j^z(0) | \Psi \rangle$ . This, however, does not hold for  $\langle S_i^x(t) S_j^x(0) \rangle$  or  $\langle S_i^y(t) S_j^y(0) \rangle$  correlation functions, which take a more complex form after the transformation.

Our approach to solving the Hamiltonian  $\mathcal{H}$  is illustrated in Figure 8. To address the sign problem, we project the Hamiltonian onto the Wannier space and employ the transformation introduced by Wang. This transformation effectively flips the sign of the  $xy$ -term in the Hamiltonian without altering the thermodynamic properties or the  $\langle S_i^z(t) S_j^z(0) \rangle$  correlation functions. While implementing an efficient QMC algorithm under the constraints of  $\mathcal{W}$  implied a significant computational challenge, we bypass this difficulty by solving the non-frustrated XXZ Hamiltonian and neglecting second-order corrections in  $J_{xy}$ . The validity of this approximation is demonstrated by the results discussed in the following sections.

#### IV. MODEL VALIDATION

As discussed in the previous section, the current model predicts three BKT transitions at zero field. Each BKT

transition is expected to produce a broad peak in the specific heat, consistent with the sequence of three peaks observed in our heat capacity data shown in Figure 4. The two upper BKT transition temperatures,  $T_{\text{BKT},1}$  and  $T_{\text{BKT},2}$ , are on the order of 10 K and 1 K, respectively, with the lowest transition at  $T_{\text{BKT},3} \approx 0.35$  K. Although the system is technically three-dimensional, and the upper two transitions are replaced by a single phase transition at  $T_{c1} \simeq T_{\text{BKT},1}$ , the corresponding anomaly in the specific heat is too weak to be detectable. As a result, the specific heat curve is well approximated by the 2D model. These results are also in good agreement with the finite-temperature Lanczos results presented in [51] for the same model. The weaker onset of XY ordering at  $T_{c2} \simeq T_{\text{BKT},3} \approx 0.35$  K is more clearly observed in Figure 9, where a slight elbow marks the transition.

To further validate the proposed spin Hamiltonian and the low-energy model derived in the previous section, we compute the specific heat curve  $C_v(T, H)$  in the low-temperature regime for the different values of the magnetic field  $\mu_0 H$ , as well as the uniform magnetization curve  $M(H)$ , up to the values corresponding to the onset of the 1/3 magnetization plateau.

As shown in Figure 3, the calculated magnetization curve is in good agreement with the experimental data, predicting a critical field  $\mu_0 H_c \approx 0.85$  T, which matches well with the observed value. Although the theoretical calculation shows a slightly non-linear increase of  $M$  with  $H$ , which is characteristic of 2D systems but seems to be absent in the measured curve. We note that LSWT theory predicts a slightly lower critical field  $\mu_0 H_c = 0.71$  T.

The specific heat  $C_v = R \partial_T \langle \mathcal{H} \rangle$  is computed for  $\mu_0 H = 0, 0.25$  and  $0.5$  T and temperatures in the interval  $0.16 \text{ K} < T < 3.27 \text{ K}$ . The lowest temperature reached by QMC calculations is slightly higher than the experimental value ( $T = 0.12 \text{ K}$ ). This limitation, combined with finite-size effects, likely explains the minor discrepancies observed in comparisons with experimental data.

The comparison with the experiment is presented in Figure 9. The phonon and Schottky contributions were subtracted from the measured data as in Figure 4(b). The above-mentioned low-temperature broad peaks are successfully reproduced by the QMC simulations of the low-energy effective model confirming the validity of the Hamiltonian parameters of  $\text{K}_2\text{Co}(\text{SeO}_3)_2$ . Moreover, as shown in Figure 10, the low-energy model also reproduces the temperature dependence of the magnetic entropy as it approaches the Wannier value.

## V. QUANTUM SPIN DYNAMICS AND INELASTIC NEUTRON SCATTERING

In this section, we present and analyze high-resolution, low-energy inelastic neutron scattering data collected in the spin supersolid phase under an applied magnetic field. We first examine the experimental neutron scattering results, then compare these findings with the QMC sim-

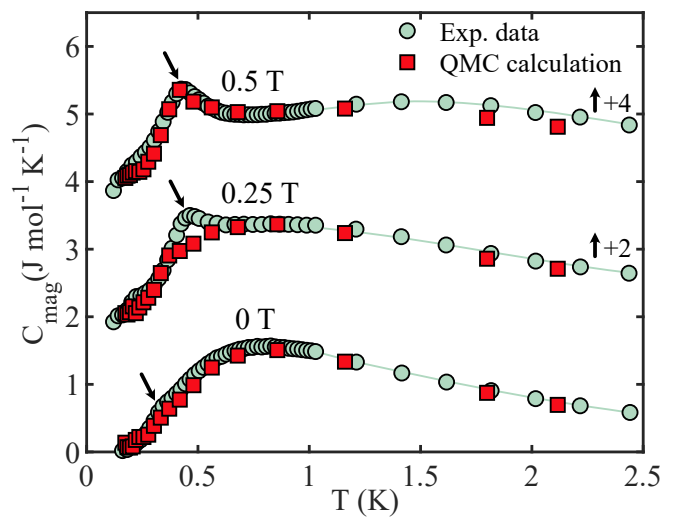


FIG. 9. Magnetic specific heat of  $\text{K}_2\text{Co}(\text{SeO}_3)_2$  for different fields  $\mu_0 H = 0, 0.25$  and  $0.5$  T applied along the  $c$  axis. Circles: experimental data from Ref. [28] with phonon and nuclear contribution subtracted as described in the text. The line is a guide for the eye. Squares: QMC calculations (this work). The black arrows indicate the BEC transition.

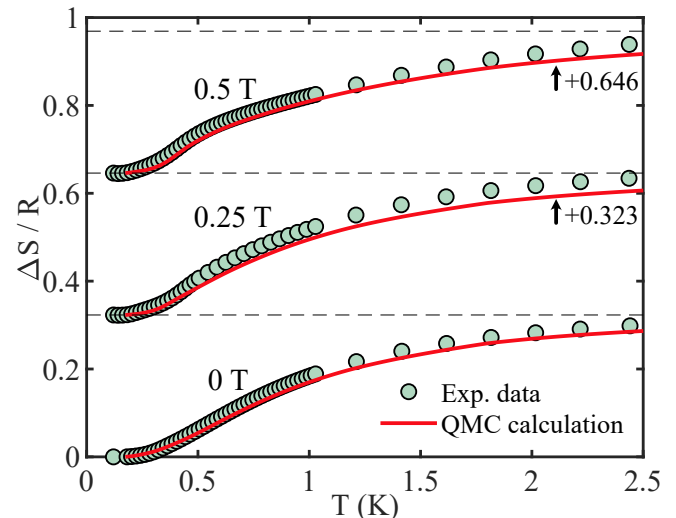


FIG. 10. Temperature dependence of magnetic entropy at  $\mu_0 H = 0, 0.25$  and  $0.5$  T. Circles: experimental data obtained by integrating the measured magnetic heat capacity  $C_{\text{mag}}/T$ . Red lines: QMC calculation. The dashed lines indicate the Wannier entropy.

ulations, and conclude by presenting and discussing the high-energy excitations at zero magnetic fields.

In Figure 5 we show the low-energy magnetic excitation spectrum of  $\text{K}_2\text{Co}(\text{SeO}_3)_2$  measured by high-resolution inelastic neutron scattering at AMATERAS as a function of energy and high-symmetry directions in the reciprocal space at  $T = 70 \text{ mK}$  and zero magnetic field. The incident neutron energy is  $E_i = 1.69 \text{ meV}$  giving a resolution of  $23 \mu\text{eV}$  at elastic scattering (to be compared



to the resolution  $\Delta E \approx 36 \mu\text{eV}$  for the data reported in [28]). To enhance the counting statistics of the neutron intensity, the data has been averaged over equivalent paths in the reciprocal space accessible in the experiment, as shown in Figure 20. The spectrum is dominated by the broad, gapless continuum of excitations, deviating drastically from the predictions of the linear spin wave theory (magnon dispersion in solid lines), and no sharp, coherent magnon modes can be resolved even with the improved energy resolution.

This is more obvious in the energy-dependent cuts plotted in Figure 11 at several representative wave vectors: M point [Figure 11(b)], half way between the K and M points [Figure 11(c)], and half way between the M and  $\Gamma$  points [Figure 11(e)]. A sharp excitation feature may be present at the lower boundary of the continuum for these wave vectors, whereas it can not be resolved at the wave vector halfway between the  $\Gamma$  and K point [Figure 11(d)]. Note that the intensity of the scattered neutrons is plotted in the logarithmic scale, and the corresponding plots with linear scale are displayed in the insets. The observation of a sharp feature at the lower boundary of a continuum of excitations in low-dimensional quantum magnets is often interpreted as a bound state of fractionalized spin excitations [52]. In the present study, we cannot resolve any gap between the sharp excitation and the rest of the continuum within our experimental resolution, which seems to support such a scenario. Nevertheless, one can never exclude the possibility that there exist closely spaced coherent magnon modes where the difference in energy is much smaller than our experimental resolution. Even then, our high-resolution INS data imposed strong constraints on the upper limit of the energy spacing between potential discrete magnon modes. Further, our data allow us to make an accurate estimate on the spectral weight contributions of the sharp magnon modes, if existing, at the lower boundary of the continuum. At the wave vectors investigated [Figure 11(b),(c),(e)], the weight of the sharp excitation (represented by a shaded Gaussian in which FWHM corresponds to the energy resolution) is only about 40%, implying that at least 60% of the total spectral weight is contributed by the continuum.

At the K point, in addition to the gapless Goldstone excitations as expected from the spontaneously broken  $U(1)$  symmetry in the supersolid phase, a gapped excitation is observed at approximately  $E \approx 0.06 \text{ meV}$  [Figure 11(a)]. This excitation corresponds to the previously described pseudo-Goldstone mode and is prominently visible in the energy-momentum plot of the magnetic excitation spectrum near the K point, as illustrated in the inset of Figure 5.

To better understand the nature of the continuum of excitations in the supersolid phase of  $\text{K}_2\text{Co}(\text{SeO}_3)_2$ , we have investigated their evolution in a magnetic field applied along the magnetic easy axis (i.e.  $c$  axis) at LET. In Figure 12 (a)-(d), we show the false-color plots of the energy-momentum cuts of the low-energy magnetic exci-

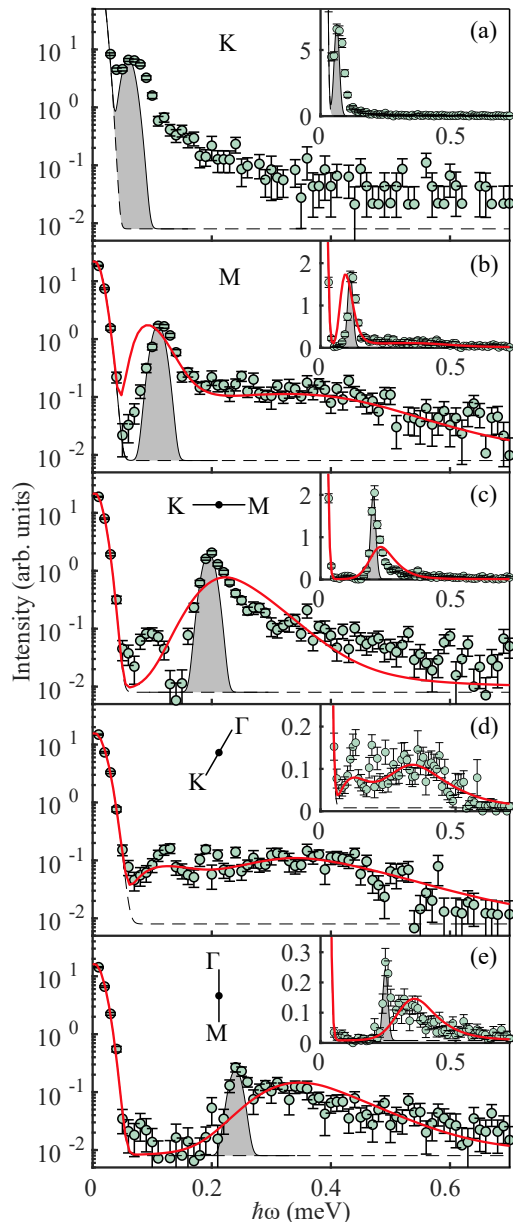


FIG. 11. Energy cuts through the INS data shown in Figure 5 at representative wave vectors as indicated. Both longitudinal and transverse spin fluctuations contribute to scattering, the intensity being proportional to  $S^{zz}(\mathbf{q}, \omega) + S^{\perp}(\mathbf{q}, \omega)$ . (a) K point, (b) M point, (c) half way between K and M, (d) half way between  $\Gamma$  and K, and (e) half way between M and  $\Gamma$ . The solid lines represent QMC calculations for  $S^{zz}(\mathbf{q}, \omega)$  only. An arbitrary global scale factor is applied to match the intensity of the M point. The measured spectra have been averaged over equivalent wave vectors accessible in the experiment. Note the y-axis is in logarithmic scale. Insets show the same plot with y-axis in linear scale. Shaded Gaussians represent the energy resolution. The dashed lines are fits to a constant background and the elastic incoherent scattering peak.

tation spectra measured at  $T = 50 \text{ mK}$  and in a field of

$\mu_0 H = 0, 0.25, 0.5,$  and  $0.75$  T, respectively. The spectra were plotted after subtracting the background scattering from the sample environment measured at  $\mu_0 H = 7$  T (note there is no magnetic excitation below 1 meV at 7 T). As before, to enhance the counting statistics, the spectra presented have been averaged over equivalent paths in the reciprocal space as illustrated in Figure 21. Typical averaged energy-dependent cuts of the spectra at the K and M points are shown in Figure 13. The energy resolution of this dataset ( $\Delta E = 40 \mu\text{eV}$ ) is lower than that obtained at AMATERAS [Figure 5 and Figure 11]. While the low-energy spectrum at zero magnetic field [Figure 12(a) and Figure 13(a)] appears qualitatively similar in both measurements, the application of a magnetic field drastically reconstructs the excitation spectrum. To emphasize the distinctions from LSWT, Figure 18 illustrates the dynamical spin structure factor (DSSF) calculated using this approach.

As shown in Figures 12(b) and 13(b), an excitation branch with a gap of  $E = 0.16$  meV at the K point becomes visible with a field of just 0.25 T, while the gapless Goldstone mode persists as expected. The splitting between these two branches is prominent near the K point, whereas they appear to remain nearly degenerate at the M point [Figure 13(f)].

The roton-like dispersion minimum of the zero-field gapless branch [Figure 12(a)] is progressively suppressed with increasing magnetic field [Figure 12(b)], consistent with the system becoming more semi-classical as it approaches the  $1/3$  magnetization plateau. In contrast, the dip at the M point persists for the gapped branch [Figure 12(b)]. Another indication of the system's evolution towards a semi-classical regime is the field-induced suppression of the zero-field dip in the lower boundary of the continuum, located halfway between the  $\Gamma$  and K points [see Figure 12(a) and Figure 5]. This dip, absent in the spin-wave theory predictions shown by solid lines, is completely suppressed at  $\mu_0 H = 0.25$  T [Figure 12(b)]. Consistent with this observation, Figure 12(b) also demonstrates that the excitations become sharper and more intense as they approach the  $\Gamma$  point. While LSWT accurately reproduces the slope of the excitations in the  $E \rightarrow 0$  limit at both the  $\Gamma$  and K points, notable discrepancies arise between the measured and predicted excitations at higher energies.

At  $\mu_0 H = 0.5$  T, the magnetic excitation spectrum undergoes further reconstruction, as shown in Figure 12(c). The gapped excitation at the K point shifts to a higher energy of 0.26 meV [see also Figure 13(c)]. Most remarkably, the continuum of excitations moves towards higher energy with increasing magnetic field, and appears to be associated with the gapped excitation branch. Moreover, the degeneracy at the M point is completely lifted, with the energy of the excitation in the gapped branch increasing to 0.35 meV [Figure 13(g)]. The roton-like dip in the gapped branch becomes hardly visible [Figure 12(c)]. Overall, the excitation intensity becomes much weaker at this field (note the  $\times 2$  factor in color scale).

Finally, the continuum of excitations disappears at  $\mu_0 H = 0.75$  T, just below the quantum phase transition to the uud plateau phase at  $\mu_0 H_c \approx 0.8$  T, as shown in Figure 12(d). The excitations evolve into sharp magnons, resembling those observed in the plateau phase at  $\mu_0 H_c = 1.5$  T, as previously reported [28]. It is worth noting that, as discussed in the previous section, LSWT predicts a lower critical field implying that the calculated magnon bands in Figure 12(d) are gapped. This reaffirms that the continuum of excitations in the supersolid state of  $\text{K}_2\text{Co}(\text{SeO}_3)_2$  is linked to the “superfluidity” of the transverse  $xy$ -moment in the Y-structure.

While the gapless branch is well described by LSWT, the gapped branch exhibits minor deviations. These discrepancies arise because LSWT is not fully accurate near the quantum critical point. Although the spin structure closely resembles the collinear uud configuration, quantum fluctuations significantly reduce the ordered moment from its saturated value [28]. Furthermore, the scattering appears diffusive: the energy width of the excitations slightly exceeds the resolution [Figure 13(h)], and weak scattering is observed at the K point near 0.5 meV, just below the gapped excitation branch [see Figure 12(d) and Figure 13(d)].

In the previous section, we validated our numerical approach by calculating the heat capacity and total magnetization and comparing the results with experimental data. We demonstrated that this methodology performs exceptionally well in accurately describing these quantities. The low-energy excited states, with energies on the order of  $E \sim J_{xy}$ , reside within the Wannier space, and it is anticipated that our approach can effectively capture these excitations as well. However, a significant limitation of our methodology is our inability to compute the  $\mathcal{S}^{xx}$  and  $\mathcal{S}^{yy}$  correlation functions. Consequently, we focus on the  $\mathcal{S}^{zz}$  component of the DSSF, defined as

$$\mathcal{S}^{zz}(\mathbf{q}, \omega) = \int_0^\infty e^{-i\omega t} \langle S_{-\mathbf{q}}^z(t) S_{\mathbf{q}}^z(0) \rangle dt \quad (10)$$

with  $S_{\mathbf{q}}^z = \frac{1}{N} \sum_j e^{-\mathbf{q} \cdot \mathbf{r}_j} S_j^z$  with  $j$  running over all lattice sites. Although a direct comparison with experimental data is not possible—since the data includes all three components of the dynamical spin structure factor—several features observed experimentally are clearly reflected in our simulations, underscoring the strong quantum origin of the magnetic excitations.

Figure 14 shows the QMC simulations for  $\mu_0 H = 0, 0.25,$  and  $0.5$  T. As these simulations are performed in imaginary time, an analytic continuation is applied to convert the data into the frequency domain. Further details about the calculations are provided in Appendix B.

The primary features of the experimental spectrum are well reproduced at zero field [Figure 14(a)]. Our simulations successfully capture the roton-like modes, and the continuum along the  $\Gamma$ -K path shows strong agreement with the experimental data. In Figure 11, we present cuts at different momenta for the zero-field calculations, emphasizing the accurate prediction of both the potential

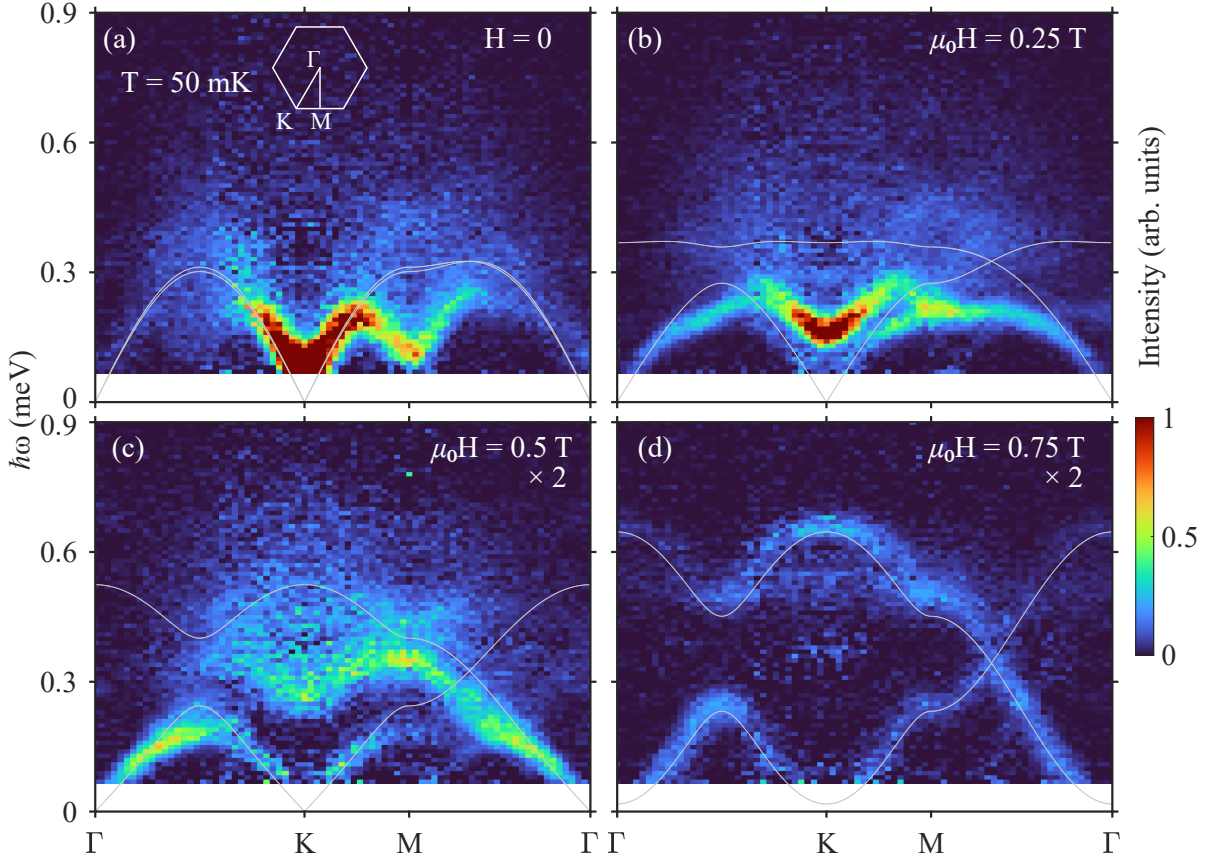


FIG. 12. False-color plots of neutron scattering intensity measured on  $\text{K}_2\text{Co}(\text{SeO}_3)_2$  on the LET spectrometer at  $T = 50$  mK as a function of energy and wave vector along high-symmetry directions of the Brillouin zone in a magnetic field applied along the  $c$  axis: (a)  $\mu_0 H = 0$ , (b) 0.25 T, (c) 0.5 T, and (d) 0.75 T. The incident neutron energy is  $E_i = 2.15$  meV, the resolution is 0.04 meV at the elastic line. The data were integrated over  $\pm 0.75$  r.l.u. in  $l$  and  $\pm 0.05$  r.l.u. in the  $(h, k, 0)$  plane perpendicular to the cut, and averaged over equivalent paths shown in Fig. 21. The spectra measured at 7 T have been subtracted to remove the background from the sample environment. Note that in (d) the residual scattering at the K point near 0.4 meV is due to spurious scattering from the cryomagnet and imperfect background subtraction. Solid lines are the dispersion curves calculated by the linear spin wave theory. The white hexagon represents the Brillouin zone boundary.  $\Gamma$ ,  $K$  and  $M$  label high symmetry points in the reciprocal space.

quasiparticle peak and the broad continuum. To ensure consistency, the intensities are rescaled to match the M point. However, a significant discrepancy with the experimental data is the absence of an extended continuum at the M point in the simulations. We conjecture that this continuum primarily originates from the  $\mathcal{S}^{xx}(\mathbf{q}, \omega)$  and  $\mathcal{S}^{yy}(\mathbf{q}, \omega)$  components of the dynamical spin structure factor, a hypothesis supported by the Lanczos results reported in [53].

The comparison becomes more challenging at finite fields, because the magnetic structure continuously evolves into the collinear up-up-down phase, implying that most of the spectral weight of  $\mathcal{S}^{zz}(\mathbf{q}, \omega)$  comes from longitudinal excitations corresponding to the two-magnon continuum, while the spectral weight from transverse modes is mainly captured by the  $\mathcal{S}^{xx}(\mathbf{q}, \omega)$  and  $\mathcal{S}^{yy}(\mathbf{q}, \omega)$  components. While this creates a noticeable discrepancy, we can still observe in Figure 14(b) a clear

energy splitting of the pseudo-Goldstone mode and the flattening of the roton minimum at  $\mu_0 H = 0.25$  T. Finally, the lower band is partially recovered at  $\mu_0 H = 0.5$  T [Figure 14(c)]. To emphasize the differences with LSWT, Figure 18 presents the dynamical spin structure factor  $\mathcal{S}^{zz}(\mathbf{q}, \omega)$  calculated within this approximation.

Lastly, we discuss the higher-energy excitations at zero field. In the pure Ising model, dispersionless single-magnon bands are predicted at energies  $E = nJ_{zz}$  with  $n = 1, 2, 3$ , corresponding to spin-flip excitations within a locally magnetized environment as illustrated in Figure 15. For  $\text{K}_2\text{Co}(\text{SeO}_3)_2$ , the excitation corresponding to  $n = 1$  has been observed at about 3 meV in zero magnetic field, using incident neutron energy  $E_i = 7.73$  meV, as shown in Figure 16. The data, averaged over equivalent reciprocal space paths [Figure 22], reveals that this excitation becomes slightly dispersive due to the nonzero  $J_{xy}$  ( $\alpha \approx 0.07$ ), with the bottom of the branch located

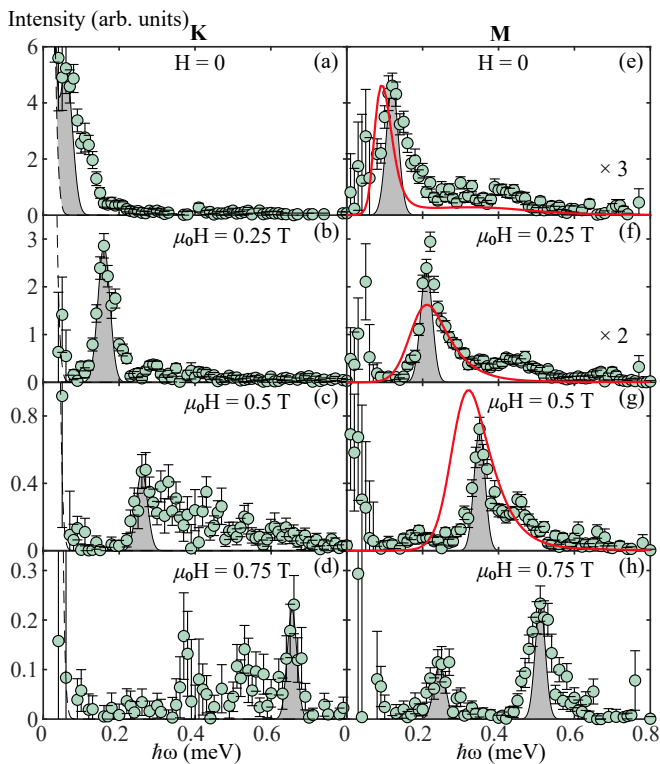


FIG. 13. Magnetic field evolution of the neutron scattering intensity in  $\text{K}_2\text{Co}(\text{SeO}_3)_2$ , as measured at the LET spectrometer with  $E_i = 2.15$  meV, as a function of energy transfer at the (a-d) K point and (e-h) M point. A magnetic field of  $\mu_0H = 0, 0.25, 0.5$ , and  $0.75$  T, respectively, is applied along the crystallographic  $c$  axis. The spectra have been averaged over equivalent wave vectors accessible in the experiment. The spectra measured at 7 T have been subtracted to remove the background from the sample environment. Note in (d) the scattering near 0.4 meV is spurious and due to imperfect background subtraction. The scale on the y-axis is linear. The shaded Gaussians represent the calculated energy resolution. The solid lines represent QMC calculations for  $S^{zz}(\mathbf{q}, \omega)$  only. An arbitrary global scale factor is applied to match the intensity of the M point at  $H = 0$ . The dashed lines are fits to the elastic peak.

at the K point. The average energy of the mode is consistent with the exchange interaction  $J_{zz} = 3.1$  meV, as deduced from high-field magnetization data [28]. Instead of a sharp coherent mode, this excitation manifests as a gapped continuum, with its broadening attributed to strong quantum fluctuations within the Wannier sector. Similar to the lower-energy modes, a sharp excitation might exist at the lower bound of the continuum, as suggested by the shaded Gaussians in the energy-dependent cuts plotted in Figure 17.

## VI. DISCUSSION

In the previous sections, we demonstrated that the XXZ Hamiltonian given in Eq. (1) and the corresponding

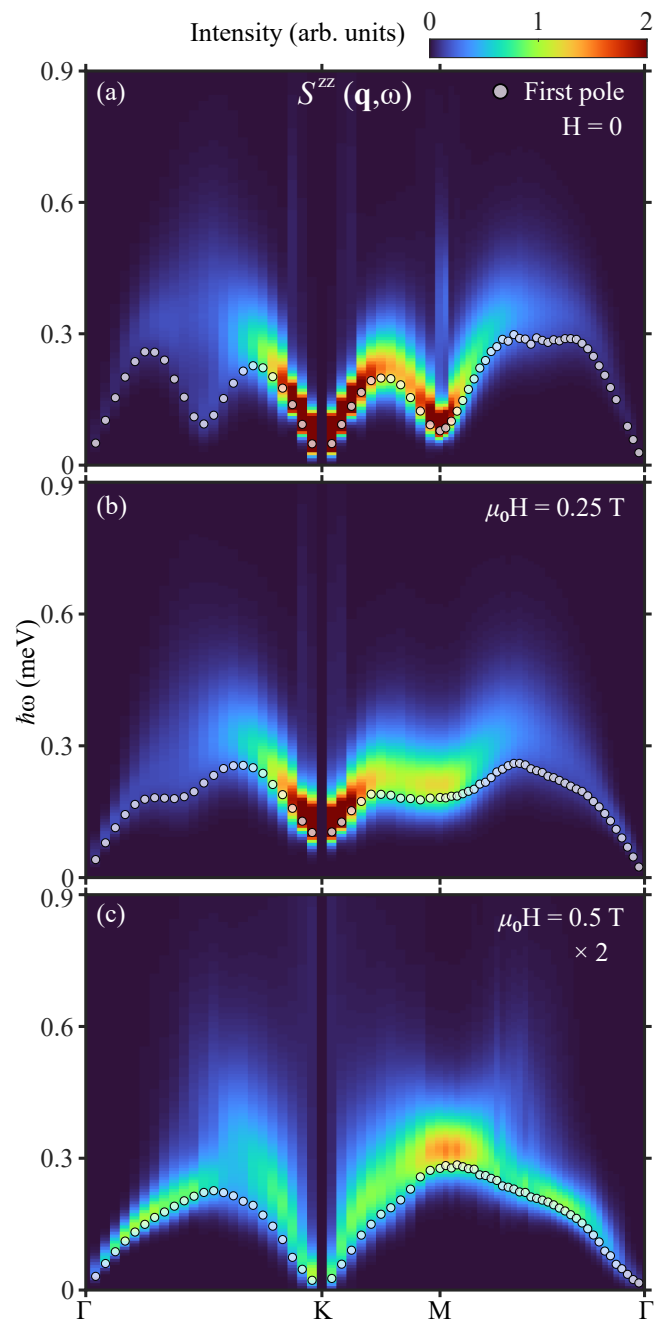


FIG. 14.  $S^{zz}$  component of the dynamical spin structure factor computed with QMC and analytic continuation for (a)  $\mu_0H = 0$  T, (b)  $\mu_0H = 0.25$  T and (c)  $\mu_0H = 0.5$  T. The white dots are the first poles of  $S^{zz}$  extracted with the method presented in Appendix B.

low-energy theory valid in the small  $J_{xy}/J_{zz}$  limit accurately describe the low-temperature magnetic properties of  $\text{K}_2\text{Co}(\text{SeO}_3)_2$ . While we cannot completely rule out additional interactions, the good agreement between theory and experiment suggests that such terms are likely very weak and would only become relevant at extremely low temperatures or energy scales. Therefore, at the energy scales studied, we can conclude with reasonable

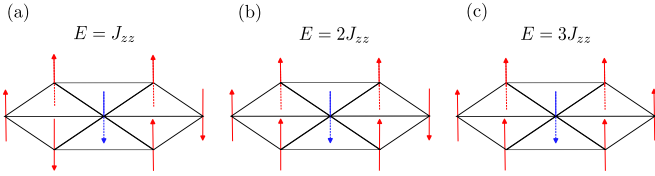


FIG. 15. Sketch of the high-energy excitations in the Ising model at zero field. The excitation corresponds to a flip in the central blue spin changing the net magnetization in  $\pm 1$  and the energy in (a)  $J_{zz}$ ; (b)  $2J_{zz}$ ; (c)  $3J_{zz}$ .

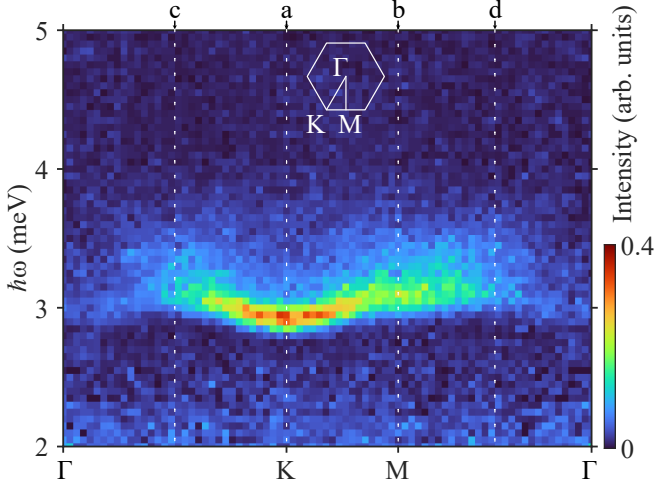


FIG. 16. (a) False-color plot of neutron scattering intensity measured on  $\text{K}_2\text{Co}(\text{SeO}_3)_2$  at the AMATERAS spectrometer with  $E_i = 7.73$  meV at  $T = 70$  mK and  $H = 0$ , as a function of energy and wave vector transfers along high-symmetry directions in the Brillouin zone. The energy resolution is 0.24 meV at the elastic position. The data were integrated over  $\pm 0.5$  r.l.u. in  $l$  and  $\pm 0.05$  r.l.u. in the  $(h, k, 0)$  plane perpendicular to the cut, and averaged over equivalent paths shown in Figure 22. No background has been subtracted. White hexagon represents the Brillouin zone boundary.  $\Gamma$ , K and M label high symmetry points in the reciprocal space. Labels above the top axis indicate the positions of energy-cuts shown in Figure 17.

confidence that  $\text{K}_2\text{Co}(\text{SeO}_3)_2$  exhibits a spin-supersolid phase, which can be described by a nearest-neighbor XXZ Hamiltonian with strong easy-axis anisotropy. The validation of this model opens the door to exploring new questions like: What is the nature of the continuum of low-energy excitations? Can this continuum be described with a renormalized semi-classical theory by resumming higher order corrections in  $1/S$  [54] or it is associated with weakly confined spinon excitations which are better described by large- $N$  approaches [55]?

A few theoretical works [56–58] have recently studied a structurally similar triangular lattice antiferromagnet  $\text{Na}_2\text{BaCo}(\text{PO}_4)_2$ , which can be described by the same easy axis XXZ Hamiltonian [13]. The ground state of  $\text{Na}_2\text{BaCo}(\text{PO}_4)_2$  has also been proposed to be a similar spin supersolid with the “Y” structure [13, 59], and the

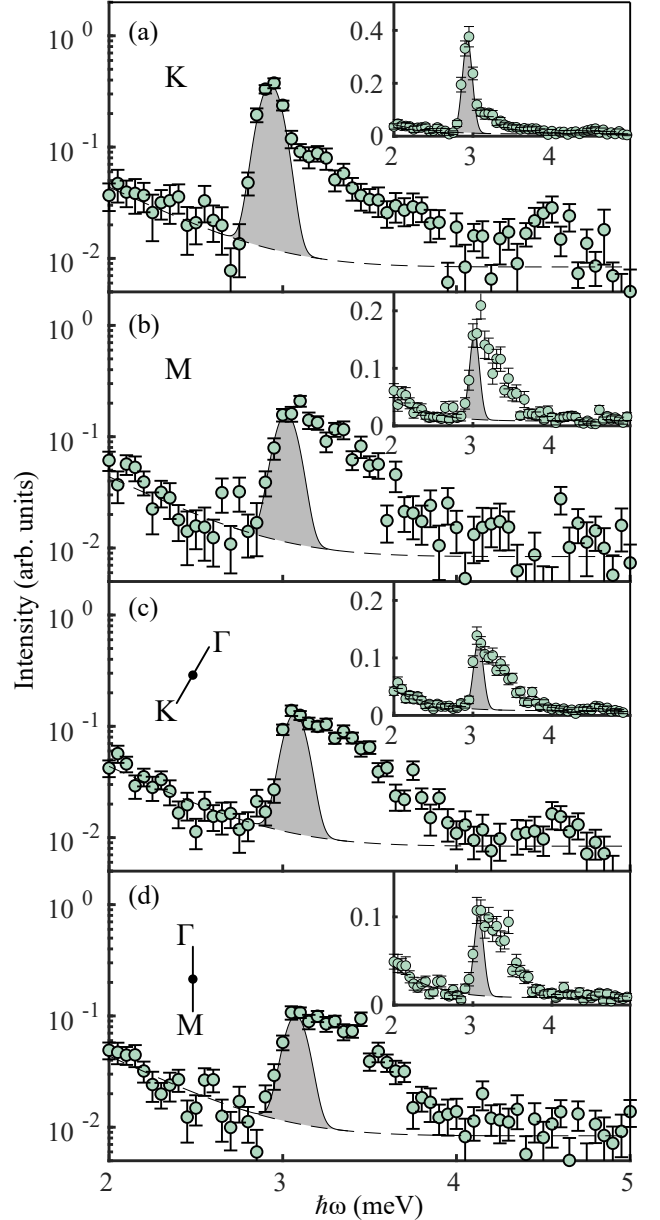


FIG. 17. Energy-cuts through the INS data shown in Figure 16 at representative wave vectors: (a) K point, (b) M point, (c) half way between  $\Gamma$  and K, and (d) half way between M and  $\Gamma$ . The wave vectors are indicated in Figure 16 by arrows. The spectra have been averaged over equivalent wave vectors. Note the y-axis is in logarithmic scale. The inset shows the same plot with a y-axis on a linear scale. The shaded Gaussian represents the energy resolution. The dashed lines are empirical fits to the background.

magnetic excitations measured by inelastic neutron scattering show a broad continuum [60]. The difference is that in  $\text{Na}_2\text{BaCo}(\text{PO}_4)_2$  the exchange anisotropy ratio  $\alpha \approx 0.6$  which is further away from the Ising limit compared with  $\text{K}_2\text{Co}(\text{SeO}_3)_2$  ( $\alpha \approx 0.07$ ), and the exchange interactions are much weaker with  $J_{zz} = 0.125$  meV

[60, 61]. Nevertheless, we may still gain some insights on the nature of the scattering continuum in  $\text{K}_2\text{Co}(\text{SeO}_3)_2$  by comparing our measured spectra with the theoretically predicted ones qualitatively.

One proposed scenario suggests that the spin supersolid ground state is a precursor to a Dirac spin liquid [56]. In this framework, the continuum of excitations arises from fractionalized spinons in the spin liquid state. The calculated excitation spectrum is qualitatively similar to the experimental observations: a continuum of excitations bounded by linear dispersion at the K and  $\Gamma$  points. The calculated constant-energy slice of the magnetic spectrum shows excitation pockets centered not only at the  $\Gamma$  and K points, but also near the M point and the wave vector halfway between  $\Gamma$  and K [28]. However, at the M point, we experimentally observe a gapped, roton-like dip instead of a gapless excitation with linear dispersion. If the system is indeed in the proximity of a U(1) Dirac quantum spin liquid, one must observe a softening of the roton-mode upon approaching the “quantum melting point”.

Other theoretical works offer alternative interpretations. Using tensor network methods, the magnetic excitation spectrum of the spin supersolid reveals various discrete magnon modes that are very close in energy. The observed continuum of excitations is then attributed to the finite experimental energy resolution [57, 58]. The calculated low-energy magnon modes exhibit a peculiar double magnon-roton structure: the lowest-energy magnon mode consists of a gapless Goldstone mode at the K point and a roton-like dip in dispersion at the M point, while the second-lowest energy magnon mode shows a gapped pseudo-Goldstone mode at the K point and another roton-like dip at the M point, nearly degenerate with the lowest branch. The former is attributed to fluctuations perpendicular to the plane of the ordered moment (purely transverse), while the latter is associated with fluctuations in the plane of the “Y” structure. This matches our observations in  $\text{K}_2\text{Co}(\text{SeO}_3)_2$  [see Figure 5 inset and Figure 11(a), (b)]. In  $\text{Na}_2\text{BaCo}(\text{PO}_4)_2$ , the pseudo-Goldstone mode is predicted to be around 0.01 meV [58], which is extremely difficult to identify experimentally. In contrast, in  $\text{K}_2\text{Co}(\text{SeO}_3)_2$ , thanks to the high energy resolution of AMATERAS, the pseudo-Goldstone mode as low as 0.06 meV can be resolved [Figure 11(a)].

While experimentally we cannot resolve the two nearly degenerate roton-like modes predicted by theory at the M point in zero magnetic field [57, 58], their presence is clearly supported by their distinct field dependence. It has been predicted that the roton-like dip in the gapless excitation branch with the Goldstone mode vanishes quickly for increasing magnetic field, whereas that associated with the gapped pseudo-Goldstone branch persists until the field-induced quantum phase transition to the uud phase [58]. As shown in Figs. 12(b) and (c), this also agrees well with our experimental observation. The diminished visibility of the roton dip at 0.5 T may stem

from its shallowing as the magnetic field increases, making it more challenging to discern experimentally. Theoretically, it has been proposed that the roton modes in the pseudo-Goldstone branch arise due to a magnon-Higgs scattering mechanism [58, 62], while those in the gapless Goldstone branch result from energy level repulsion imposed by the former. This explains its disappearance under a magnetic field, as the pseudo-Goldstone branch shifts to higher energy [see Figure 12 (c)].

Finally, we discuss the gapped continuum near 3 meV. Since  $\text{Na}_2\text{BaCo}(\text{PO}_4)_2$  ( $\alpha = 0.6$ ) is much further from the Ising limit compared to  $\text{K}_2\text{Co}(\text{SeO}_3)_2$  ( $\alpha = 0.07$ ), such excitations due to spin-flips are not present in the theories mentioned above. However, in a more recent theory for  $\text{K}_2\text{Co}(\text{SeO}_3)_2$  [63], such an excitation is indeed reproduced. Still, the transformation of the sharp, flat, dispersive-less spin-flip excitation in a pure Ising system into a continuum as the system deviates slightly from the Ising limit arises from the quantum fluctuations within the Wannier manifold induced by  $J_{xy}$ . If these excitations were due to closely spaced magnon modes, the energy difference would have to fall below our experimental resolution. The low-energy excitations have also been studied within the same theoretical framework, with the roton-like dip at the M point predicted. However, the calculated spectrum is broadened by an energy resolution of 0.05 meV, making a quantitative comparison with our high-resolution data challenging.

## VII. CONCLUSION

The XXZ triangular lattice model, in all its simplicity, is home to a plethora of very interesting and fundamental many-body quantum phenomena. It is exceedingly rare to find a realization of such an important theoretical construct in a real material as exact, as what we have in  $\text{K}_2\text{Co}(\text{SeO}_3)_2$ . Moreover, it is very rare that a spin system where all the exotic physics stems from strong geometric frustration can be studied, and that on a quantitative level, with QMC.  $\text{K}_2\text{Co}(\text{SeO}_3)_2$  also stands out in that, by virtue of being in the strong-Ising limit, it gives us this unique opportunity.

## ACKNOWLEDGMENTS

We thank James Neuhaus for the useful discussion in the setup of SmoQyDEAC.jl. This work was Supported by a MINT grant of the Swiss National Science Foundation. Data at J-PARC were collected in Experiment no. 2023B0161. Experiments at the ISIS Pulsed Neutron and Muon Source were supported by a beamtime allocation from the Science and Technology Facilities Council under proposal no. RB2320138. L. M. Ch. was supported by the U.S. Department of Energy, Office of Science, Basic Energy Sciences, Materials Science and Engineering Division.

### Appendix A: Dynamical spin structure factor computed by LSWT

Figure 18 shows the total (left) and  $\mathcal{S}^{zz}$  component (right) of the dynamical spin structure factor computed using linear spin-wave theory.

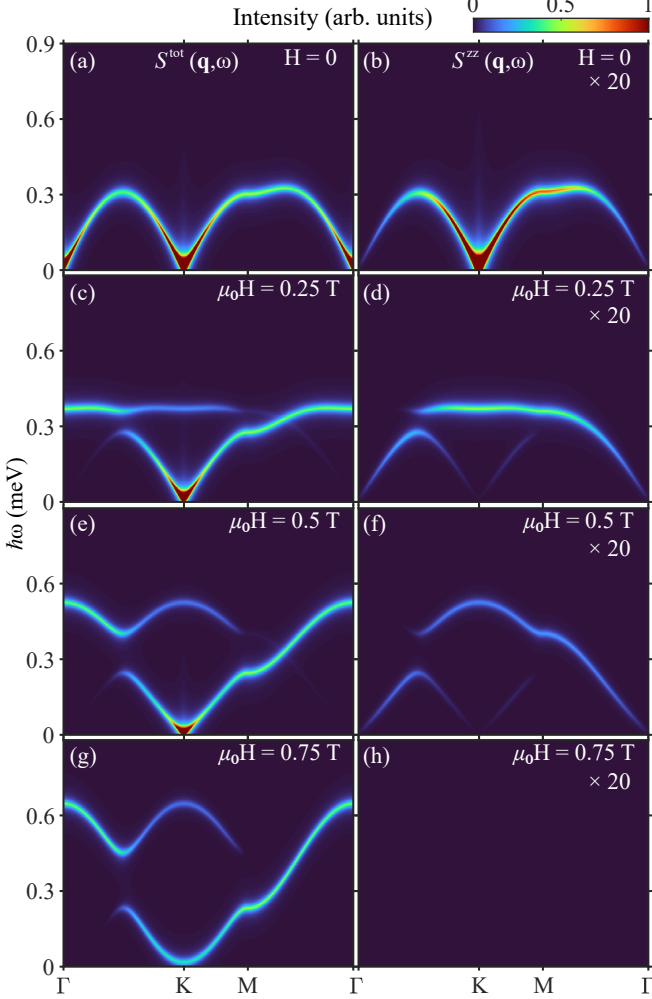


FIG. 18. Total and  $\mathcal{S}^{zz}$  component of the dynamical spin structure factor computed by linear spin wave theory for (a),(b)  $H = 0$  T, (c),(d)  $\mu_0 H = 0.25$  T and (e),(f)  $\mu_0 H = 0.5$  T and (g),(h)  $\mu_0 H = 0.75$  T. The FWHM used in the Dirac delta functions corresponds to the experimental resolution.

### Appendix B: Details about QMC calculations of the DSSF

The QMC worm algorithm simulation enables the calculation of the imaginary-time two-point correlation function  $\mathcal{G}^{zz}(\mathbf{q}, \tau) = \langle S_{-\mathbf{q}}^z(\tau) S_{\mathbf{q}}^z(0) \rangle$ , where  $\tau$  is the imaginary time. This imaginary-time correlation function is related to the dynamical spin structure factor (DSSF)  $\mathcal{S}^{zz}(\mathbf{q}, \omega)$  via a Laplace transformation

$$\mathcal{G}^{zz}(\mathbf{q}, \tau) = \int_{-\infty}^{\infty} e^{-\omega\tau} \mathcal{S}^{zz}(\mathbf{q}, \omega) d\omega. \quad (\text{B1})$$

Since detailed balance dictates that  $\mathcal{S}_{-\mathbf{q}}^{zz}(-\omega) = e^{-\beta\omega} \mathcal{S}_{\mathbf{q}}^{zz}(\omega)$ , and we are interested in a problem with spatial inversion symmetry,  $\mathcal{S}_{-\mathbf{q}}^{zz}(\omega) = \mathcal{S}_{\mathbf{q}}^{zz}(\omega)$ , the integration in Eq. B1 can be restricted to positive frequencies,

$$\mathcal{G}^{zz}(\mathbf{q}, \tau) = \int_0^{\infty} K(\omega, \tau) \mathcal{S}^{zz}(\mathbf{q}, \omega) d\omega, \quad (\text{B2})$$

with

$$K(\omega, \tau) = \left( e^{-\tau\omega} + e^{-(\beta-\tau)\omega} \right). \quad (\text{B3})$$

The inversion problem is non-trivial due the ill-posed nature of inverting Eq. B2, meaning that there is no unique solution. As a first approximation, we can use a saddle point approximation of Eq. B2, which extracts the frequency of the lowest energy pole of  $\mathcal{S}^{zz}(\mathbf{q}, \omega)$ . The frequency component of  $\mathcal{G}^{zz}(\mathbf{q}, \tau)$  is the sole survivor in the asymptotically long imaginary time:

$$\mathcal{G}^{zz}(\mathbf{q}, \tau) \approx A_{\mathbf{q}} \left( e^{-\tau\omega^*} + e^{-(\beta-\tau)\omega^*} \right) \quad \text{as } \tau \rightarrow \beta \quad (\text{B4})$$

$A_{\mathbf{q}}$  and  $\omega^*$  represent fitting parameters associated with the residue and frequency of the pole, respectively. These parameters are acquired through a non-linear fitting process [see Figure 19] [64].

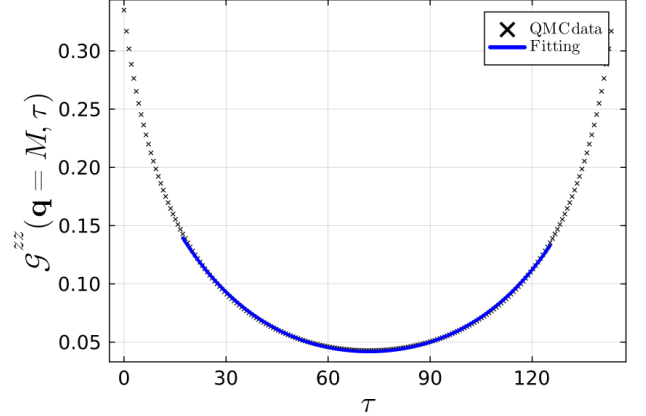


FIG. 19. Non-linear fitting Eq. B4 for QMC data for two  $\mathbf{q} = M$ . Since we are interested in the behavior on the long imaginary time  $\tau \rightarrow \beta$  a cutoff is imposed on the data fitting process.

To attack the problem of inverting Eq. B2, we employ the “Differential Evolution Algorithm” introduced and implemented in [42, 43]. After applying this procedure, the data is convoluted with the experimental resolution.

### Appendix C: Reciprocal paths

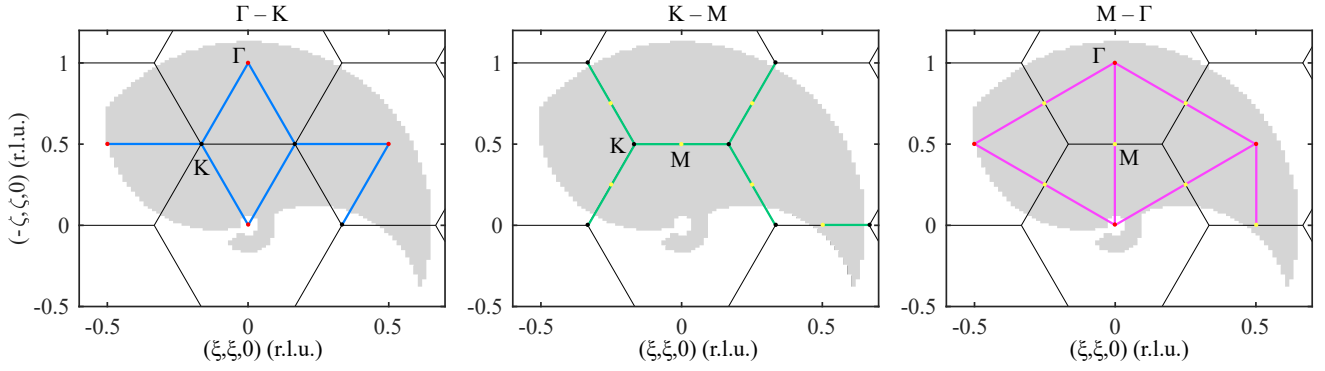


FIG. 20. Schematic diagram showing the equivalent reciprocal space paths (a)  $\Gamma$ -K, (b) K-M, and (c) M- $\Gamma$ , used to plot the averaged excitation spectrum in Figure 5. The shaded area is the reciprocal space covered by the detector bank at AMATERAS with  $E_i = 1.69$  meV. Black hexagons represent the Brillouin zone boundaries.

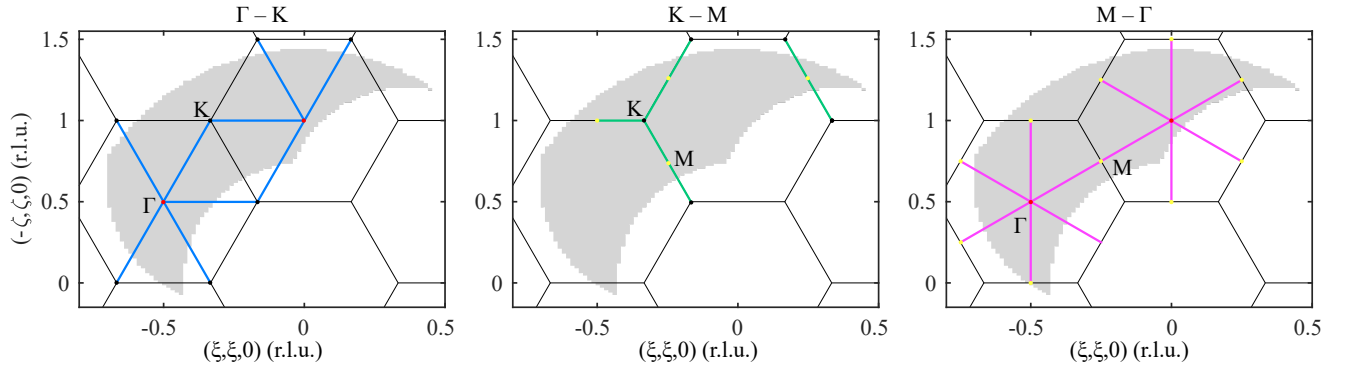


FIG. 21. Schematic diagram showing the equivalent reciprocal space paths (a)  $\Gamma$ -K, (b) K-M, and (c) M- $\Gamma$ , used to plot the averaged excitation spectrum in Figure 12. Shaded area is the reciprocal space covered by the detector bank at LET with  $E_i = 2.15$  meV. Black hexagons represent the Brillouin zone boundaries.

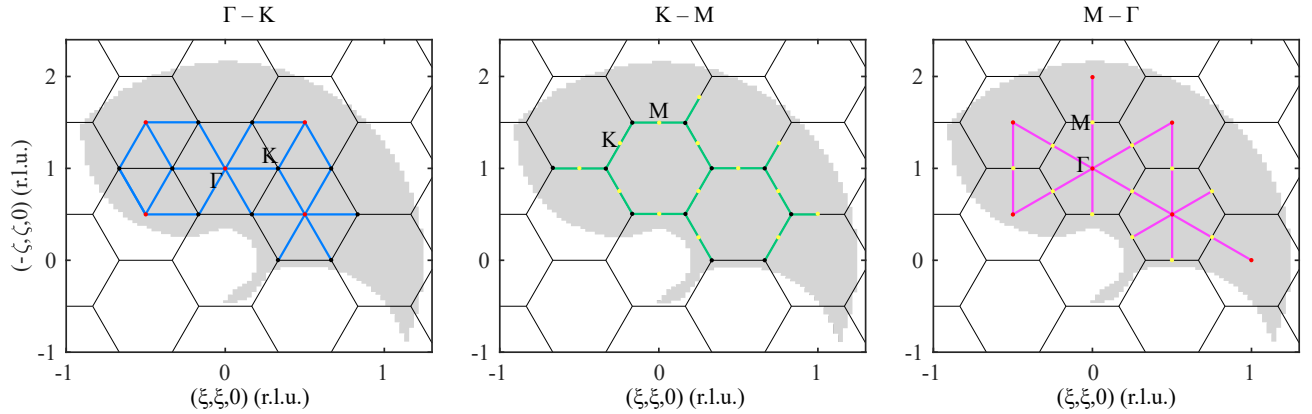


FIG. 22. Schematic diagram showing the equivalent reciprocal space paths (a)  $\Gamma$ -K, (b) K-M, and (c) M- $\Gamma$ , used to plot the averaged excitation spectrum in Figure 16. The shaded area is the reciprocal space covered by the detector bank at AMATERAS with  $E_i = 7.73$  meV. Black hexagons represent the Brillouin zone boundaries.

[1] M. Boninsegni and N. V. Prokof'ev, Colloquium: Super-solids: What and where are they?, *Rev. Mod. Phys.* **84**,



- [2] A. J. Leggett, Can a solid be “superfluid”?, *Phys. Rev. Lett.* **25**, 1543 (1970).
- [3] A. F. Andreev and I. M. Lifshitz, Quantum theory of defects in crystals, *Soviet Physics Uspekhi* **13**, 670 (1971).
- [4] J.-R. Li, J. Lee, W. Huang, S. Burchesky, B. Shteynas, F. Ç. Top, A. O. Jamison, and W. Ketterle, A stripe phase with supersolid properties in spin-orbit-coupled Bose-Einstein condensates, *Nature* **543**, 91 (2017).
- [5] L. Tanzi, S. M. Roccuzzo, E. Lucioni, F. Famà, A. Fioretti, C. Gabbanini, G. Modugno, A. Recati, and S. Stringari, Supersolid symmetry breaking from compressional oscillations in a dipolar quantum gas, *Nature* **574**, 382 (2019).
- [6] M. Guo, F. Böttcher, J. Hertkorn, J.-N. Schmidt, M. Wenzel, H. P. Büchler, T. Langen, and T. Pfau, The low-energy Goldstone mode in a trapped dipolar supersolid, *Nature* **574**, 386 (2019).
- [7] D. Heidarian and K. Damle, Persistent supersolid phase of hard-core bosons on the triangular lattice, *Phys. Rev. Lett.* **95**, 127206 (2005).
- [8] S. Wessel and M. Troyer, Supersolid hard-core bosons on the triangular lattice, *Phys. Rev. Lett.* **95**, 127205 (2005).
- [9] R. G. Melko, A. Paramekanti, A. A. Burkov, A. Vishwanath, D. N. Sheng, and L. Balents, Supersolid order from disorder: Hard-core bosons on the triangular lattice, *Phys. Rev. Lett.* **95**, 127207 (2005).
- [10] T. Momoi and K. Totsuka, Magnetization plateaus of the Shastry-Sutherland model for  $\text{SrCu}_2(\text{BO}_3)_2$ : spin-density wave, supersolid, and bound states, *Phys. Rev. B* **62**, 15067 (2000).
- [11] P. Sengupta and C. D. Batista, Spin supersolid in an anisotropic spin-one Heisenberg chain, *Phys. Rev. Lett.* **99**, 217205 (2007).
- [12] F. Heydarinasab and J. Abouie, Spin supersolid phase in coupled alternating spin chains, *Scientific Reports* **8**, 7955 (2018).
- [13] Y. Gao, Y.-C. Fan, H. Li, F. Yang, X.-T. Zeng, X.-L. Sheng, R. Zhong, Y. Qi, Y. Wan, and W. Li, Spin supersolidity in nearly ideal easy-axis triangular quantum antiferromagnet  $\text{Na}_2\text{BaCo}(\text{PO}_4)_2$ , *npj Quantum Materials* **7**, 89 (2022).
- [14] J. Wang, H. Li, N. Xi, Y. Gao, Q.-B. Yan, W. Li, and G. Su, Plaquette singlet transition, magnetic barocaloric effect, and spin supersolidity in the Shastry-Sutherland model, *Phys. Rev. Lett.* **131**, 116702 (2023).
- [15] S. Miyashita, Magnetic properties of Ising-like Heisenberg antiferromagnets on the triangular lattice, *Journal of the Physical Society of Japan* **55**, 3605 (1986).
- [16] D. Yamamoto, G. Marmorini, and I. Danshita, Quantum phase diagram of the triangular-lattice XXZ model in a magnetic field, *Phys. Rev. Lett.* **112**, 127203 (2014).
- [17] D. Sellmann, X.-F. Zhang, and S. Eggert, Phase diagram of the antiferromagnetic XXZ model on the triangular lattice, *Phys. Rev. B* **91**, 081104 (2015).
- [18] P. Sengupta and C. D. Batista, Field-induced supersolid phase in spin-one Heisenberg models, *Phys. Rev. Lett.* **98**, 227201 (2007).
- [19] P. Sengupta and C. D. Batista, Spin supersolid in an anisotropic spin-one Heisenberg chain, *Phys. Rev. Lett.* **99**, 217205 (2007).
- [20] K. P. Schmidt, J. Dorier, A. M. Läuchli, and F. Mila, Supersolid phase induced by correlated hopping in spin-1/2 frustrated quantum magnets, *Phys. Rev. Lett.* **100**, 090401 (2008).
- [21] G. H. Wannier, Antiferromagnetism. the triangular Ising net, *Phys. Rev.* **79**, 357 (1950).
- [22] T. Matsubara and H. Matsuda, A Lattice Model of Liquid Helium, I, *Progress of Theoretical Physics* **16**, 569 (1956).
- [23] F. Wang, F. Pollmann, and A. Vishwanath, Extended supersolid phase of frustrated hard-core bosons on a triangular lattice, *Phys. Rev. Lett.* **102**, 017203 (2009).
- [24] D. Heidarian and A. Paramekanti, Supersolidity in the triangular lattice spin-1/2 XXZ model: A variational perspective, *Phys. Rev. Lett.* **104**, 015301 (2010).
- [25] C. A. Gallegos, S. Jiang, S. R. White, and A. L. Chernyshev, *Phase Diagram of the Easy-Axis Triangular-Lattice  $J_1$ - $J_2$  Model* (2024), arXiv:2412.03648 [cond-mat].
- [26] J. Alicea, A. V. Chubukov, and O. A. Starykh, Quantum stabilization of the 1/3-magnetization plateau in  $\text{Cs}_2\text{CuBr}_4$ , *Phys. Rev. Lett.* **102**, 137201 (2009).
- [27] Y. Kamiya, L. Ge, T. Hong, Y. Qiu, D. L. Quintero-Castro, Z. Lu, H. B. Cao, M. Matsuda, E. S. Choi, C. D. Batista, M. Mourigal, H. D. Zhou, and J. Ma, The nature of spin excitations in the one-third magnetization plateau phase of  $\text{Ba}_3\text{CoSb}_2\text{O}_9$ , *Nature Communications* **9**, 2666 (2018).
- [28] M. Zhu, V. Romerio, N. Steiger, S. D. Nabi, N. Murai, S. Ohira-Kawamura, K. Y. Povarov, Y. Skourski, R. Sibille, L. Keller, Z. Yan, S. Gvasaliya, and A. Zheludev, Continuum excitations in a spin supersolid on a triangular lattice, *Phys. Rev. Lett.* **133**, 186704 (2024).
- [29] T. Chen, A. Ghasemi, J. Zhang, L. Shi, Z. Tagay, L. Chen, E.-S. Choi, M. Jaime, M. Lee, Y. Hao, H. Cao, B. Winn, R. Zhong, X. Xu, N. P. Armitage, R. Cava, and C. Broholm, Phase diagram and spectroscopic evidence of supersolids in quantum ising magnet  $\text{K}_2\text{Co}(\text{SeO}_3)_2$  (2024), arXiv:2402.15869 [cond-mat.str-el].
- [30] R. Zhong, S. Guo, and R. J. Cava, Frustrated magnetism in the layered triangular lattice materials  $\text{K}_2\text{Co}(\text{SeO}_3)_2$  and  $\text{Rb}_2\text{Co}(\text{SeO}_3)_2$ , *Phys. Rev. Mater.* **4**, 084406 (2020).
- [31] P. Anderson, Resonating valence bonds: A new kind of insulator?, *Materials Research Bulletin* **8**, 153 (1973).
- [32] L. Balents, Spin liquids in frustrated magnets, *Nature* **464**, 199 EP (2010).
- [33] L. Savary and L. Balents, Quantum spin liquids: a review, *Reports on Progress in Physics* **80**, 016502 (2016).
- [34] C. Broholm, R. J. Cava, S. A. Kivelson, D. G. Nocera, M. R. Norman, and T. Senthil, Quantum spin liquids, *Science* **367**, eaay0668 (2020).
- [35] E. A. Ghioldi, S.-S. Zhang, Y. Kamiya, L. O. Manuel, A. E. Trumper, and C. D. Batista, Evidence of two-spinon bound states in the magnetic spectrum of  $\text{Ba}_3\text{CoSb}_2\text{O}_9$ , *Phys. Rev. B* **106**, 064418 (2022).
- [36] M. Wildner, Isotypism of a selenite with a carbonate: structure of the buetschliite-type compound  $\text{K}_2\text{Co}(\text{SeO}_3)_2$ , *Acta Crystallographica Section C* **48**, 410 (1992).
- [37] K. Nakajima, S. Ohira-Kawamura, T. Kikuchi, M. Nakamura, R. Kajimoto, Y. Inamura, N. Takahashi, K. Aizawa, K. Suzuya, K. Shibata, T. Nakatani, K. Soyama, R. Maruyama, H. Tanaka, W. Kambara, T. Iwahashi, Y. Itoh, T. Osakabe, S. Wakimoto, K. Kakurai, F. Maekawa, M. Harada, K. Oikawa, R. E. Lechner, F. Mezei, and M. Arai, Amateras: A cold-neutron disk chopper spectrometer, *Journal of the Physical Society of Japan* **80**, SB028 (2011).
- [38] R. Ewings, A. Buts, M. Le, J. van Duijn, I. Bustinduy, and T. Perring, Horace: Software for the analysis

- of data from single crystal spectroscopy experiments at time-of-flight neutron instruments, *Nuclear Instruments and Methods in Physics Research Section A: Accelerators, Spectrometers, Detectors and Associated Equipment* **834**, 132 (2016).
- [39] K. Barros, S. Matin, Y. W. Li, M. Wilson, and U. O. of Science, Contributing to sunny open source code (2022).
- [40] Y. Kato and N. Kawashima, Quantum Monte Carlo method for the Bose-Hubbard model with harmonic confining potential, *Phys. Rev. E* **79**, 021104 (2009).
- [41] Y. Motoyama, K. Yoshimi, A. Masaki-Kato, T. Kato, and N. Kawashima, DSQSS: Discrete Space Quantum Systems Solver, *Comput. Phys. Commun.* **264**, 107944 (2021).
- [42] N. S. Nichols, P. Sokol, and A. Del Maestro, Parameter-free differential evolution algorithm for the analytic continuation of imaginary time correlation functions, *Phys. Rev. E* **106**, 025312 (2022).
- [43] J. Neuhaus, N. S. Nichols, D. Banerjee, B. Cohen-Stead, T. A. Maier, A. D. Maestro, and S. Johnston, Smoqydeac.jl: A differential evolution package for the analytic continuation of imaginary time correlation functions (2024), [arXiv:2407.04568](https://arxiv.org/abs/2407.04568) [cond-mat.stat-mech].
- [44] B. Kleine, E. Müller-Hartmann, K. Frahm, and P. Fazekas, Spin-wave analysis of easy-axis quantum antiferromagnets on the triangular lattice, *Zeitschrift für Physik B Condensed Matter* **87**, 103 (1992).
- [45] Q. Sheng and C. L. Henley, Ordering due to disorder in a triangular heisenberg antiferromagnet with exchange anisotropy, *Journal of Physics: Condensed Matter* **4**, 2937 (1992).
- [46] J. V. José, L. P. Kadanoff, S. Kirkpatrick, and D. R. Nelson, Renormalization, vortices, and symmetry-breaking perturbations in the two-dimensional planar model, *Phys. Rev. B* **16**, 1217 (1977).
- [47] P. Sengupta, A. W. Sandvik, and R. R. P. Singh, Specific heat of quasi-two-dimensional antiferromagnetic heisenberg models with varying interplanar couplings, *Phys. Rev. B* **68**, 094423 (2003).
- [48] J. G. Rau, P. A. McClarty, and R. Moessner, Pseudo-Goldstone gaps and order-by-quantum disorder in frustrated magnets, *Phys. Rev. Lett.* **121**, 237201 (2018).
- [49] A. Sen, P. Dutt, K. Damle, and R. Moessner, Variational wave-function study of the triangular lattice supersolid, *Physical Review Letters* **100**, 147204 (2008).
- [50] F. Wang, F. Pollmann, and A. Vishwanath, Extended supersolid phase of frustrated hard-core bosons on a triangular lattice, *Phys. Rev. Lett.* **102**, 017203 (2009).
- [51] M. Ulaga, J. Kokalj, A. Wietek, A. Zorko, and P. Prelovšek, Finite-temperature properties of the easy-axis Heisenberg model on frustrated lattices, *Phys. Rev. B* **109**, 035110 (2024).
- [52] M. B. Stone, D. H. Reich, C. Broholm, K. Lefmann, C. Rischel, C. P. Landee, and M. M. Turnbull, Extended Quantum Critical Phase in a Magnetized Spin-1/2 Antiferromagnetic Chain, *Phys. Rev. Lett.* **91**, 037205 (2003).
- [53] M. Ulaga, J. Kokalj, and P. Prelovšek, Easy-axis Heisenberg model on the triangular lattice: from supersolid to gapped solid, [arXiv:2408.05034](https://arxiv.org/abs/2408.05034) (2024).
- [54] A. L. Chernyshev and M. E. Zhitomirsky, Spin waves in a triangular lattice antiferromagnet: Decays, spectrum renormalization, and singularities, *Phys. Rev. B* **79**, 144416 (2009).
- [55] E. A. Ghioldi, M. G. Gonzalez, S.-S. Zhang, Y. Kamiya, L. O. Manuel, A. E. Trumper, and C. D. Batista, Dynamical structure factor of the triangular antiferromagnet: Schwinger boson theory beyond mean field, *Phys. Rev. B* **98**, 184403 (2018).
- [56] H. Jia, B. Ma, Z. Wang, and G. Chen, Quantum spin supersolid as a precursory dirac spin liquid in a triangular lattice antiferromagnet (2023), [arXiv:2304.11716](https://arxiv.org/abs/2304.11716) [cond-mat.str-el].
- [57] Y. Gao, C. Zhang, J. Xiang, D. Yu, X. Lu, P. Sun, W. Jin, G. Su, and W. Li, Spin supersolid phase and double magnon-roton excitations in a cobalt-based triangular lattice (2024), [arXiv:2404.15997](https://arxiv.org/abs/2404.15997) [cond-mat.str-el].
- [58] R. Chi, J. Hu, H.-J. Liao, and T. Xiang, Dynamical spectra of spin supersolid states in triangular antiferromagnets (2024), [arXiv:2404.14163](https://arxiv.org/abs/2404.14163) [cond-mat.str-el].
- [59] J. Xiang, C. Zhang, Y. Gao, W. Schmidt, K. Schmalzl, C.-W. Wang, B. Li, N. Xi, X.-Y. Liu, H. Jin, G. Li, J. Shen, Z. Chen, Y. Qi, Y. Wan, W. Jin, W. Li, P. Sun, and G. Su, Giant magnetocaloric effect in spin supersolid candidate Na<sub>2</sub>BaCo(PO<sub>4</sub>)<sub>2</sub>, *Nature* **625**, 270 (2024).
- [60] J. Sheng, L. Wang, W. Jiang, H. Ge, N. Zhao, T. Li, M. Kofu, D. Yu, W. Zhu, J.-W. Mei, Z. Wang, and L. Wu, Continuum of spin excitations in an ordered magnet (2024), [arXiv:2402.07730](https://arxiv.org/abs/2402.07730) [cond-mat.str-el].
- [61] J. Sheng, L. Wang, A. Candini, and L. Wu, Two-dimensional quantum universality in the spin-1/2 triangular-lattice quantum antiferromagnet Na<sub>2</sub>BaCo(PO<sub>4</sub>)<sub>2</sub>, *PNAS* **119**, e2211193119 (2022).
- [62] M. Powalski, G. S. Uhrig, and K. P. Schmidt, Roton minimum as a fingerprint of magnon-Higgs scattering in ordered quantum antiferromagnets, *Phys. Rev. Lett.* **115**, 207202 (2015).
- [63] Y. Xu, J. Hasik, B. Ponsioen, and A. H. Nevidomskyy, Simulating spin dynamics of supersolid states in a quantum Ising magnet (2024), [arXiv:2405.05151](https://arxiv.org/abs/2405.05151) [cond-mat.str-el].
- [64] Z. Zhang, K. Wierschem, I. Yap, Y. Kato, C. D. Batista, and P. Sengupta, Phase diagram and magnetic excitations of anisotropic spin-one magnets, *Phys. Rev. B* **87**, 174405 (2013).